Submitted for publication in the Astrophysical Journal

A Gas Giant Circumbinary Planet Transiting an Evolved F Star Primary of the Eclipsing Binary Star KIC 4862625 and the Independent Discovery and Characterization of the two transiting planets in the Kepler-47 System.

V. B. Kostov[1,2], P. R. McCullough[2], T. C. Hinse[3,4], Z. I. Tsvetanov[1], G. Hébrard[5,6], R. F. Díaz[7], M. Deleuil[7], J. A. Valenti[2]

vkostov@pha.jhu.edu

ABSTRACT

We report the discovery of a transiting, gas giant circumbinary planet orbiting the eclipsing binary KIC 4862625 and describe our independent discovery of the two transiting planets orbiting Kepler-47 (Orosz et al. 2012). We describe a simple and semi-automated procedure for identifying individual transits in light curves and present our follow-up measurements of the two circumbinary systems. For the KIC 4862625 system, the $0.49 \pm 0.018\ r_{Jupiter}$ radius planet revolves every ~ 138 days and occults the $1.14 \pm 0.14\ M_{\odot}$, $1.59 \pm 0.06\ R_{\odot}$ F8 IV subgiant primary star producing aperiodic transits of variable durations commensurate with the configuration of the eclipsing binary star. Our best-fit model indicates the orbit has a semi-major axis of 0.56 AU and is slightly eccentric, $e = 0.1$. For the Kepler-47 system, we confirm the results of Orosz et al. (2012). Modulations in the radial velocity of KIC 4862625A are measured both spectroscopically and photometrically, i.e. via Doppler boosting, and produce similar results.

[1]Department of Physics and Astronomy, Johns Hopkins University, 3400 North Charles Street, Baltimore, MD 21218

[2]Space Telescope Science Institute, 3700 San Martin Dr., Baltimore MD 21218

[3]Armagh Observatory, College Hill, BT61 9DG Armagh, NI, UK

[4]Korea Astronomy and Space Science Institute (KASI), Advanced Astronomy and Space Science Division, Daejeon 305-348, Republic of Korea

[5]Institut dAstrophysique de Paris, UMR 7095 CNRS, Université Pierre & Marie Curie, 98bis boulevard Arago, 75014 Paris, France

[6]Observatoire de Haute-Provence, Université dAix-Marseille & CNRS, 04870 Saint Michel lObservatoire, France

[7]Laboratoire d'Astrophysique de Marseille, 38 rue Frédéric Joliot-Curie, 13388 Marseille cedex 13, France

Subject headings: binaries: eclipsing – planetary systems – stars: individual (KIC 4862625, Kepler-47) – techniques: photometric – techniques

1. Introduction

For decades the science fiction community has imagined that planets can orbit binary stars, yet only recently have such systems actually been detected. Timing variations either in the rotation period of a neutron star member of a binary system (Sigurdsson et al., 2003) or in the stellar occultations (when the two stars eclipse each other) of eight eclipsing binary (EB) systems (Deeg et al. 2008; Lee et al. 2009; Beuermann et al. 2010, 2011; Potter et al. 2011; Qian et al. 2011; Qian et al. 2012) have been interpreted as the gravitational perturbation of additional bodies on the binary stellar system, suggesting the presence of a total of 12 circumbinary (CB) planets on wide orbits with periods of tens of years.

The lower limits on the masses of all twelve objects, however, fall in the super-Jupiter regime, making their planetary nature uncertain. Furthermore, the orbital stability of some of the multi-planet circumbinary systems (HW Vir, HU Aqr and NN Ser) have been studied recently, showing that some of them are on highly unstable orbits (Horner et al. 2011; Hinse et al. 2012; Horner et al. 2012a,b; Goździewski et al. 2012; Beuermann et al. 2012).

Doyle et al. (2011) announced the first direct evidence of a Saturn-sized planet that transits both members of an EB eclipsing binary, specifically Kepler-16. Since then, five more CB planets have been announced: Saturn-sized planets that transit Kepler-34b and Kepler-35b (Welsh et al. 2012), the first Neptune-sized planet that transits Kepler-38 (Orosz et al. 2012b), and two Neptune-sized planets that transit Kepler-47 (Orosz et al. 2012). The latter system is the first binary discovered to have two planets, one Neptune-sized on a 300 day orbit and the other Earth-sized on a 49.5 day orbit.

Substantial efforts in theoretical modeling indicate that planets such as these should not be uncommon. Simulations of dynamical stability show that beyond a critical distance, CB planets can have stable orbits in practically all binary configurations. The critical distance is on the order of a few binary separations (Dvorak 1986; Holman & Weigert 1999; Scholl et al. 2007; Haghighipour et al. 2010; Schwarz et al. 2011; Doolin & Blundell 2011). The orbits of Kepler-16b, 34b, 35b and 38b are indeed outside the critical orbital semi-major axis, but only by 21%, 24%, 14% and 26% respectively (Welsh et al. 2012; Orosz et al. 2012b). Kepler-47b, while notably farther from the instability region (Orosz et al. 2012), is still not too far out, suggesting such "reaching for the limit" behavior to be typical of CB planets.

The fact that these four planets are so close to the theoretical limit for stability may suggest

that their host systems had an interesting dynamical history where migration and/or planet-planet scattering may have played a significant role in sculpting their present architecture. Formation and evolution theory of giant planets around binary stars has been studied extensively (Pierens and Nelson 2007, 2008a, 2008b), providing a number of outcomes that depend on initial conditions. Simulations of gas giants have shown that Saturn-size planets (like Kepler-16b, 34b and 35b) stabilize at a 5:1 orbital resonance and may be very common, compared to Jupiter-size planets that are either scattered out of the system or gradually drift outward into the disk. Single, Neptune-size planets (such as Kepler-38b) migrate and stop at a distance of about three times the binary stars separation, leading the authors to suggest that "the cavity edge of the precursor CB disk appears to be an excellent place to look for low mass planets in close binary systems." If there are two Neptune-size planets in the system, they become locked in a mean motion resonance, while a five-planet system is either disrupted or, in one simulation, also ends up in a resonance, implying that such multiple Neptune-size planets in resonant orbits may be indeed common. Models for the formation and evolution of terrestrial planets around binary stars (Quintana & Lissauer, 2006) have shown that, in the presence of Jupiter at 5 AU, CB terrestrial planets can readily form around a wide variety of binary systems. At least one terrestrial planet forms in all simulations presented by the authors. While the final masses of all simulated terrestrial planets vary little, the outcome for the architecture of the planetary system is very dependent on the parameters of the stellar binary. Highly eccentric binaries tend to harbor fewer, more diverse suite of planets compared to binaries with very low eccentricity, a prediction that can be addressed by the addition of more pictures to the family portrait of the five Kepler planets.

More than 20 years ago Borucki and Summers (1984) proposed monitoring EB systems to search for planets because nearly edge-on inclination significantly increases the probability transits. At the time is was not practical to monitor targets continuously over many days (Kepler-16b, for example, has an orbital period of 230 days). On March 6 of 2009, 380 years after Johannes Kepler predicted the transit of Venus across the disk of the Sun, NASA launched the appropriately named Kepler Mission to search for Earth-like planets in the habitable zone of Solar-type stars and to determine their occurrence frequency (Borucki et al. 2010). To achieve this, a 0.95 Schmidt telescope on a Heliocentric Earth trailing orbit continuously and simultaneously monitors about 150,000 stars in the visible range from 423 nm to 897 nm over a 100 square degrees patch of the sky in the Cygnus region where $\sim$ 60% of the stars are G-type stars on or near the Main Sequence. Utilizing the transit method, the instrument searches for periodic dips in the brightness of a star caused by a planet transiting across its disk. The Kepler mission has been remarkably successful in finding transiting planets, discovering more than 2300 planet candidates (Borucki et al. 2011; Batalha et al. 2012), 77 of which have been confirmed by the time of writing. Amongst this treasure throve of data are also a set of 2165 EB systems (Slawson et al. 2011), the main focus of our work.

Searching light curves of EB stars for transits of a third body is non-trivial. In addition to the significant limitations associated with intrinsic stellar variability and instrumental artifacts, CB planets have *inconstant* transit times, durations, and depths, all of which that depend on the phase of the binary system (Schneider & Chevreton 1990). To transit one of the stars, the planet must "hit a moving target" (Orosz et al. 2012). A benefit is that these transit signatures cannot be attributed to the stars themselves, to a background EB, or to other unrelated astrophysical or instrumental events, strongly supporting the CB-planet hypothesis. One challenge is that traditional transit searching algorithms, e.g. Box-fitting Least Squares (BLS) (Kovacs et al. 2002), used to detect periodic, box-like signals in the light curve of a single star are not optimized for finding transiting CB planets due to the unique nature of their signal. Several methods for the detection of transiting CB planets have been proposed. One approach is based on simulating light curves produced by an exhaustive search of possible orbits of CB-planets and fitting them to the data (Doyle et al. 2000; Ofir 2008). Carter & Agol (2012) have developed the Quasi-periodic Automated Transit Search QATS algorithm, which is similar to BLS but optimized for aperiodic pulses. QATS has been successfully applied to CB-planets. Orosz et al. (2012) report that QATS failed to detect the outer planet Kepler-47c due to decreasing sensitivity for longer periods. While transiting gas giants cause a dimming of their host star large enough to be seen by eye in light curves, the transits of smaller planets can be easily missed by visual inspection.

The initial discovery of CB transits together with the availability of exquisite Kepler data inspired us to develop a semi-automated procedure to identify aperiodic transits. We describe the procedure, which is based on the established BLS algorithm but modified and applied in a novel way. We applied it to finding transiting planets around EB stars listed in the Kepler catalog of Slawson et al. (2011). We examined the detached EB systems and identified several candidates that exhibited additional transit-like features in their light curves. Here we present the independent discoveries of two CB planets Kepler-47bc and KIC 4862625b.

In this paper, we will describe the analysis as a linear, deductive process, although it is inherently iterative, with one aspect feeding back into an earlier part. For brevity and clarity, we do not emphasize the iterations. This paper is organized as follows. In Section 2.2 we describe the procedure used to discover the two CB systems, followed by radial velocity measurements and spectra of the host stars in Section 3.2. The three-body dynamical model used to explore the parameter space of the two systems is presented in Section 7 aka 7. We present our results in Section 6, discuss them in Section 8 and draw conclusions in Section 9.

2. Kepler Photometry

2.1. Detrending

We began with the long-cadence (∼30 min) PDCSAP flux of KIC 4862625 generated by the Kepler mission for the publicly available[1] quarters 1-9. Using the ephemeris of Prša et al. (2010) and examining the phase-folded light curve, we flagged data points within 0.12 days of the centers of the primary or secondary eclipses, or within 0.5 days of the planetary transit events.[2] There were 437, 387, and 238 points in each category, respectively, corresponding to 1.26%, 1.12%, 0.69% of the total, 34681 data points. To remove the instrumental discontinuities in flux created by the quarterly rotation of the Kepler focal plane, we divide each quarter's data by its median. We flagged six points that differed from the rest by more than 0.2% in normalized flux.

The unflagged flux is sinusoidal with a period of $p_{rot} \approx 2.63$ d, which we attribute to modulation caused by the rotation of star A. To detrend the flux variations attributed to rotation, for the purposes of providing eclipse and planetary transit light curves normalized to unity, we fit a unique sine wave in the local vicinity of each of the 34681 data points, in each case using unflagged data within $p_{rot}/2$ of each data point. Each of the 34681 sine waves had a fixed period, p_{rot}, and we fit for three parameters: the mean, the amplitude, and the phase. We iterated the procedure, adjusting the value of p_{rot}, until the gradient in the phase shifts of the fitted sine waves over the entire data span was zero, indicating a best-fitted average rotational period, $p_{rot} = 2.6382 \pm 0.0037$ d, where the quoted "uncertainty" is the standard deviation of p_{rot} fit piece-wise over quarterly time spans. Finally, we divided each data point by its best-fitting sine wave evaluated at the time of each particular data point. We use the resulting detrended, normalized light curve for subsequent analysis, and we use the mean values of the sine waves for the analysis of the Doppler boosting (Section 4.4). Exclusive of flagged data, the RMS of the residuals of the detrended, normalized light curve about unity is 222 ppm.

2.2. Box-fitting Least Squares, BLS, for Single Transits

We invented a semi-automated procedure to identify individual, aperiodic transit-like features in a light curve. The procedure automatically finds square-wave or "box-shaped" features within a light curve.

---

[1] http://archive.stsci.edu/kepler/ or http://exoplanetarchive.ipac.caltech.edu .

[2] This is one example of the iterative analysis: first we detrended the light curve, then we identified the planetary transits, then we detrended the light curve again with the transit points flagged.

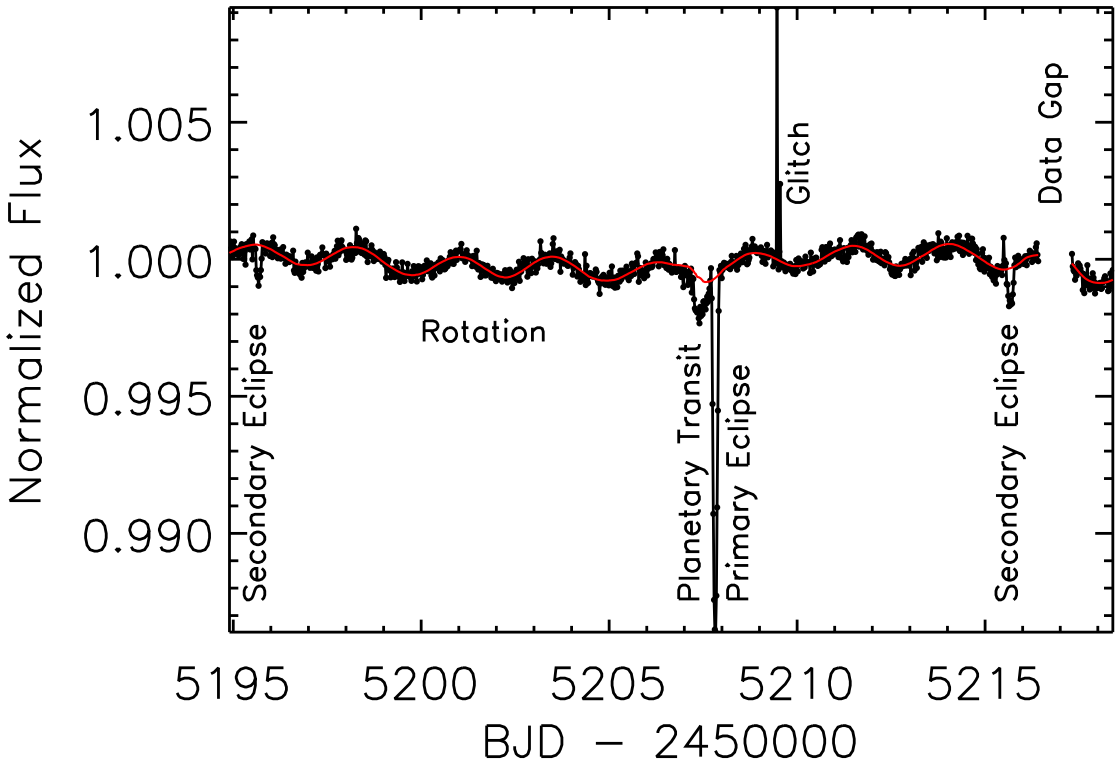

Fig. 1.— Characteristics of the light curve of KIC 4862625. A 23-day portion of the Kepler light curve illustrates various phenomena. Instrumental effects are labeled above the data; astrophysical effects are labeled below the data. We flagged two data points as a "glitch," and a gap in the data is visible at BJD = 2455217. The eccentric orbit of the EB is apparent from the fact that primary eclipse is not centered in time between the two secondary eclipses. The primary eclipse is $\sim 1.4\%$ deep. The red line illustrates the sine-wave fit to the rotational modulation of the light curve. The secondary eclipses, the planetary transit, and the 2.6-day rotational modulation all have similar amplitudes, $\sim 0.1\%$.

Using the raw EB light curves SAPFLUX from the Kepler database we first normalize them and remove the EB's eclipses using the Box-fitting Least Squares method (BLS, Kovács et al. 2002). Next we detrend the data, using only those points with a SAPQUALITY flag of 0. The detrending is non-trivial and has to be done on a target-by-target basis, as each binary star has complex baseline variability that spans timescales from hours to days. We use an iterative fit with a high-order Legendre polynomial on each quarter, further broken down into smaller segments according to the data flags.

Within each segment of the light curve, the procedure automatically identifies the center, width, and depth of the two most-significant box-shaped features, one positive and one negative. The latter is a "transit" candidate and the former is an "anti-transit." Because transits are negative features in the residuals of a detrended light curve, we can validate empirically the statistical significance of the transit candidates by comparison with the anti-transits extracted from the same data. Doing so helps us to not be overwhelmed with false-positives.

The number M of light-curve segments is not particularly critical. The segment length should be longer than any actual transit. For CB planets, in principle the transits can be as long as half an orbit of the EB, in the case where the planet and the star are traveling in parallel at nearly the same projected rate (Schneider & Chevreton 1990). Such transits will be rare and generally accompanied by shorter transits, created when the planet and star are moving in opposite directions. The segment length should be shorter than the orbital period of the planet, lest only one of two genuine transits be identified in a segment. For CB planets of P-type (Dvorak 1982), the planet's orbital period must be longer than the period of the EB, and for orbital stability the CB planet's period must be at least a few times longer than the EB's period (Section 7). From these two limits, the segment length should be between one half and a few times the orbital period of the EB. However, in practice, the intrinsic variability of the stars in the system prescribe the length of the segment. In any case, to prevent a transit being split by the segment boundaries, we analyze each light curve at least twice with the boundaries of the segments shifted.

In all cases, detrending of the light curve is crucial to our method. Very short-period EB stars, contact, and semi-detached EBs are difficult to study with our method. They are highly variable and there are few measurements in between the stellar eclipses, forcing us to use segments much larger than the binary period.

To avoid systematics effects that might mimic a transit, a merit criterion is necessary. As a convenience, one can use the BLS algorithm to find the individual transit- and anti-transit-features in segments of the detrended light curve's residuals. Because BLS is designed to find *periodic* box-like features, one option is to replicate N times the segment under study to form a periodic light curve. One can then use BLS to search for the most significant transit- and anti-transit features with that single period defined by the replication. The number N of replications is not particularly

important. To find the anti-transits, we simply invert the sign of the residuals of the light curve and search a second time. Although it would be more efficient to extract the most-significant positive and negative features in one pass, the execution time is trivial and enormously smaller than in the traditional BLS which must loop over thousands of trial periods, and smaller than the detrending also. Alternatively one can modify the original BLS computer code to analyze a single segment of unreplicated data; we have implemented each variant. The only potential difference is a tuning parameter within BLS, namely the minimum number of data points within an acceptable box-like feature, which must be adjusted commensurate with the number of replications N.

After the automated procedure identifies the M most-significant pairs of transit- and anti-transit-candidates from the M segments, we examine the ensemble for outlier transit-candidates in a manner similar to that described by Burke et al. (2006). Burke et al. validated transit-like features with an ensemble of features reported by BLS for hundreds of stars observed simultaneously. Because of the large number of observations in each star's Kepler light curve, we validate transit-like features in each light curve with the ensemble of transit- and anti-transit features from only that particular light curve.

For completeness, we briefly describe Burke's method here. Assuming dimming features (transits) and brightening features ("anti-transits") are due to systematic effects, it is reasonable to expect that there will not be a strong tendency for such effects to produce dips versus blips. In other words, typically $\delta_{(\chi^2)transit}$ will be similar to $\delta_{(\chi^2)anti-transit}$ for each segment. On the other hand, a highly significant transit signal is an outlier in a $\delta_{(\chi^2)transit}$ and $\delta_{(\chi^2)antitransit}$ diagram (Figure 2). The segments where noise dominates (black crosses) cluster in a cloud of points with similar values for $\delta_{(\chi^2)transit}$ and $\delta_{(\chi^2)anti-transit}$, but the segments containing the tertiary transits (red crosses) are well separated. As seen from the figure (and depending on the merit criterion) there can be a significant number of outliers, requiring a human eye to check the segments which triggered the routine. The number of triggers are highly dependent on the detrending of the baseline – quiet stars (like Kepler-16) have very few outlying points (planetary transits) where smaller transit signals in more variable binaries (Kepler-47) will be accompanied by a greater number of false positives.

Figures 2, 3 and 4 show examples from the light curves for KIC 4862625, Kepler-47 and Kepler-16. The three figures were presented on February 8, 2012 to a committee of Johns Hopkins University as part of the graduate student matriculation procedures for one of us (V.B.K.). As such, it used all the Kepler data that was publically-available at that time, namely Quarters 1 to 6.

To evaluate the sensitivity of our method, we insert fake transits in the light curves and study their recovery rate as a function of the transit depth. An example for Kepler-16 is shown on Figure 4 where the black crosses represents segments with zero fake transits, blue diamonds are segments dominated by systematic effects, red symbols are due to Kepler-16b and the yellow stars correspond to segments in which fake transits with a depth of 240 ppm (Earth-like signal) were

superposed. The fake transits have variable depths, durations and period to simulate that expected for a CB planet. Also they all been inserted outside the critical semimajor axis for stability in the system. One quarter of the fake transits are not recovered: some fall into data gaps, others into noisier parts of the light curve. However, for the case of Kepler-16, random simulations of the Earth-sized planet transits resulted in a 75% recovery rate, using a lower cut criteria compared to the one adopted for finding the signals of Kepler-16b. As seen from Figure 4, the inserted fakes occupy a clearly-defined cloud, well-separated from the rest, something that be used as a merit criterion of what transit signal can be recovered from that particular light curve. This shows that the described method works well for finding not only individual transits but, depending on circumstances, also for Earth-like transits of quiet stars and even for transits with durations as short as only three low-cadence Kepler samples, e.g. the quaternary eclipse of Kepler-16 represented by the red square on Figure 4.

3. Spectra

3.1. Apache Point Observatory Observations

KIC 4862625 and Kepler-47 were observed with the 3.5 m telescope at the Apache Point Observatory on four occasions between April and July, 2012. Coincidentally, the spectroscopic observations of Kepler-47 by Orosz et al. (2012) and ourselves began within 48 hours of each other. We used the medium dispersion Dual Imaging Spectrograph (DIS) in its highest resolution spectroscopic mode. The pair of B1200/R1200 gratings in combination with the $1.5''$ slit delivers a spectrum with resolution R$\sim$3000 and covering simultaneously two 1200Å windows centered on 4500Åand 6500Å, respectively. The slit was oriented along the parallactic angle. Each night we obtained one or two exposures of each target supplemented by exposures of spectrophotometric and radial velocity standards. Nightly we also obtained several HeNeAr lamp spectra for wavelength calibration, and we used telluric lines in the observed spectra to correct for offsets due to flexure or other instrumental effects. Conditions of all four nights were not strictly photometric. Each target was observed for $\sim$900 seconds per night, yielding a peak signal to noise ratio in the continuum of 20 to 30 per resolution element.

The data reduction included bias and flat-field correction, aperture extraction, wavelength and flux calibration. We compared the APO long-slit spectrum of KIC 4862625 with a library of stellar spectra (Pickles 1998). For the R$\sim$3000 APO spectra, the FWHM $\sim$45 km s^{-1} broadening evident in the SOPHIE spectra (Section 3.2) is unresolved. We estimate from the shape of the continuum and strengths of particular spectral lines that the best match is spectral type F8 IV. The subgiant classification is consistent with the density of star A determined later from the light curve and

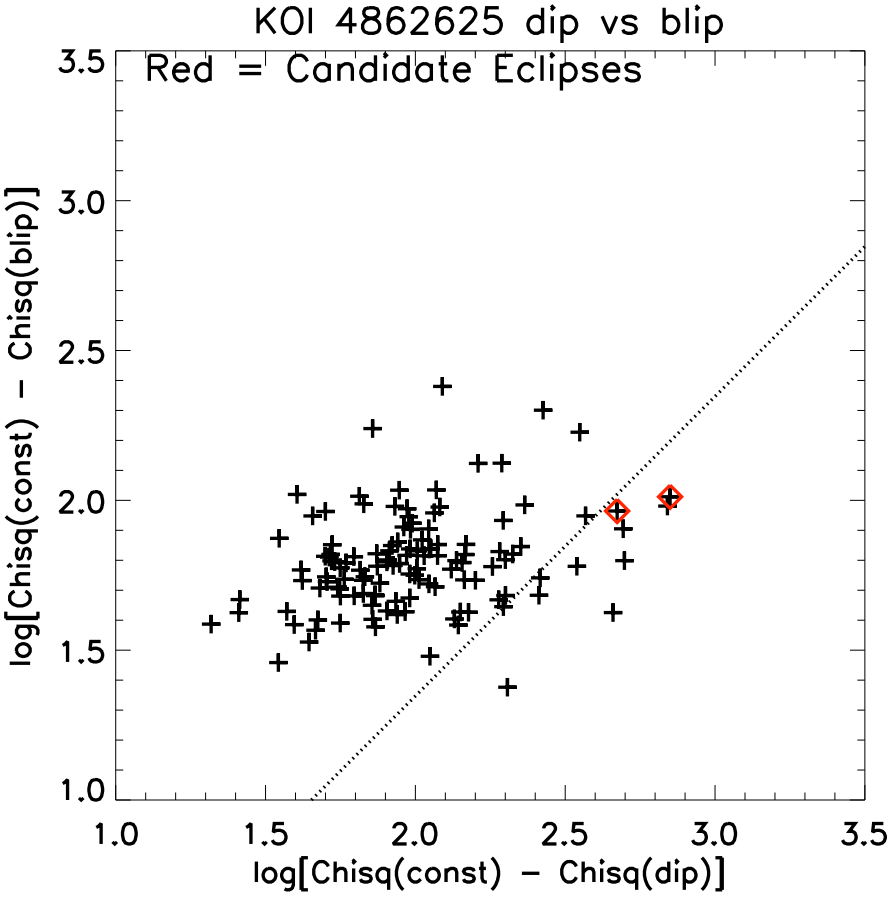

Fig. 2.— The transit/anti-transit diagram for KIC 4862625.

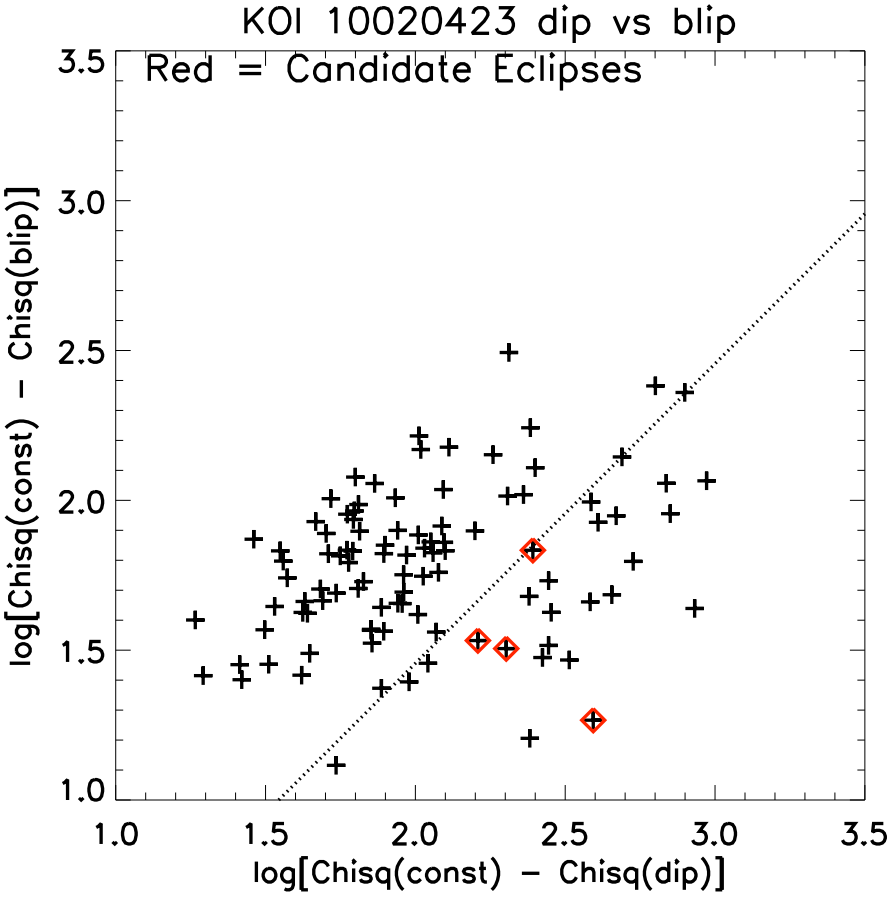

Fig. 3.— The transit/anti-transit diagram for KIC 10020423, a.k.a. Kepler-47.

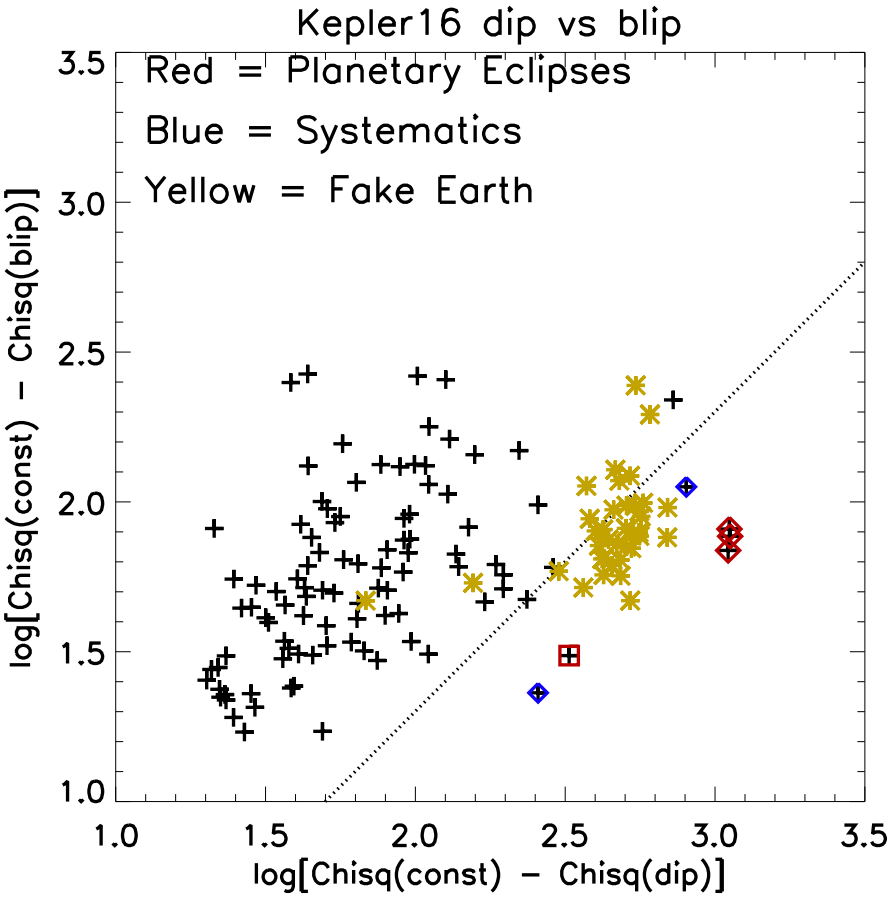

Fig. 4.— The transit/anti-transit diagram for Kepler-16 with simulated transits of an Earth-sized planet superposed (yellow).

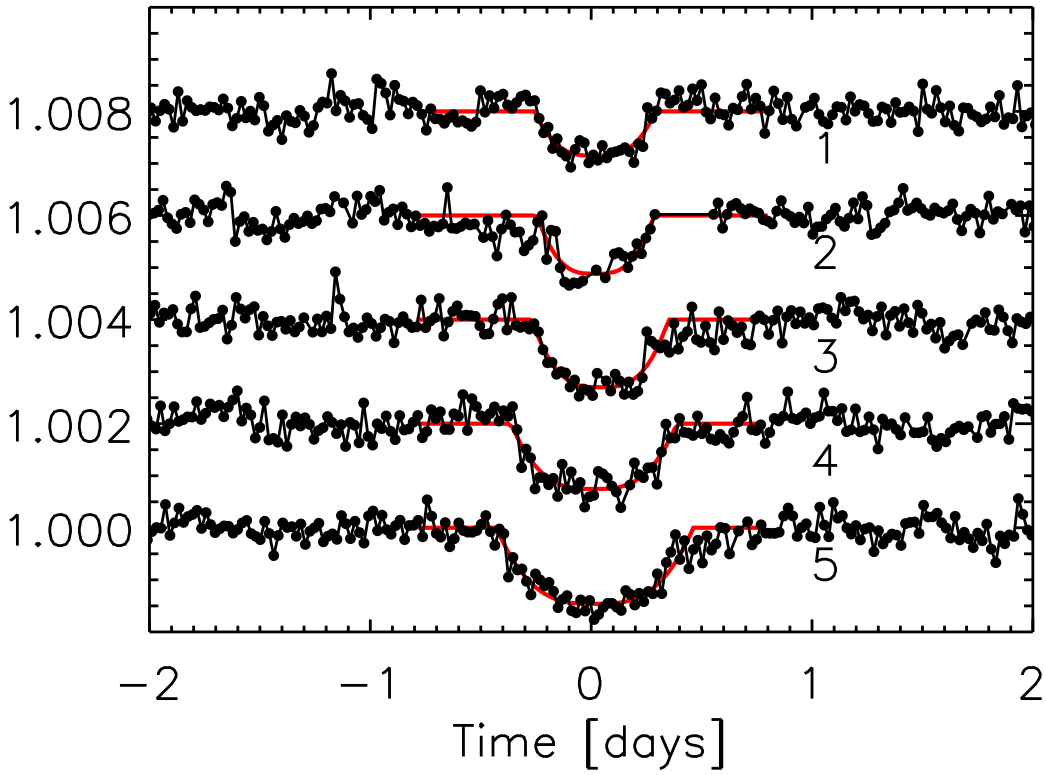

Fig. 5.— Planetary transits of KIC 4862625. The normalized and detrended flux centered on the five planetary transit events are shown (top to bottom, labeled 1, ..., 5), along with model fits. Events 1 to 4 have been offset vertically for clarity. A primary eclipse immediately after egress of event 2 has been excised from the plot for clarity.

the mass function. The Kepler Input Catalog (KIC) tends to over estimate log(g) for subgiants, especially those hotter than about 5400 K, which can lead to underestimates of their radii in the KIC, typically by factors of 1.5 to 2 (Brown et al. 2011). For KIC 4862625, the KIC radius estimate is 0.806 $R_\odot$, indeed approximately half the size that we estimate in this work.

3.2. SOPHIE observations and data reduction

The two targets were observed at the end of summer 2012 with the SOPHIE spectrograph at the 1.93-m telescope of Haute-Provence Observatory, France. The goal was to detect the reflex motion of the primary stars due to their secondary components through radial velocity variations. SOPHIE (Bouchy et al. 2009) is a fiber-fed, cross-dispersed, environmentally stabilized echelle spectrograph dedicated to high-precision radial velocity measurements. For such binary systems the amplitudes of variation are expected to be of the order of a few to a few tens $\mathrm{km\,s^{-1}}$, which is well in SOPHIE capabilities despite the faintness of the targets. The data were secured in High-Efficiency mode (resolution power $R = 40\,000$) and slow read-out mode of the detector. In order to reach signal-to-noise ratio per pixel of the order of 10 at 550 nm, exposure times ranged between 1200 and 2000 sec for Kepler-47, and between 500 and 900 sec for KIC 4862625.

The spectra were extracted from the detector images with the SOPHIE pipeline, which includes localization of the spectral orders on the 2D-images, optimal order extraction, cosmic-ray rejection, wavelength calibration and corrections of flat-field. Then we performed a cross-correlation of the extracted spectra with a G2-type numerical mask including more than 3500 lines, and finally measures the radial velocities from Gaussian fits of the cross-correlation functions (CCFs) and the associated photon-noise errors, following the method described by Baranne et al. (1996) and Pepe et al. (2002). For Kepler-47 and KIC 4862625 respectively, the full widths at half maximum of those Gaussians are 12 ± 1 $\mathrm{km\,s^{-1}}$ and 15 ± 2 $\mathrm{km\,s^{-1}}$, and their contrasts are $17 \pm 4\,\%$ and $4 \pm 2\,\%$ of the continua. One of the observations of KIC 4862625 was made at the twilight: the pollution due to the bright sky background was corrected thanks to the reference fiber pointed on the sky (e.g. Hébrard et al. 2008). Other exposures were not polluted by sky background nor Moon light. In Table 9 the SOPHIE radial velocities are absolute in barycentric reference, whereas the APO radial velocities are absolute for KIC 4862625 and relative for Kepler-47.

Radial velocity variations in phase with the Kepler ephemeris are clearly detected. Section 4.3 addresses the orbital parameters derived from the radial velocities in combination with the light curve. Section 4.2 addresses atmospheric parameters of star A derived from the spectra.

4. Data Analysis

4.1. Eclipsing Binary Light Curve

The light curve of the EB star constrains the *relative* orbit of the two stars: the orbital period P, the center times of primary eclipse T_t and secondary eclipse T_o, the semi-major axis of the relative orbit in units of the radius of star A, a/r_A, and the orbital inclination, i. Also from the light curve, we derive the relative radii of the two stars, $k = r_B/r_A$, and the fraction of the flux in the Kepler bandpass[3] emitted by star B, f_B. Nominally, we assume zero "third light," so $f_A = 1 - f_B$; we examine that assumption later in this section. We adopt the period $P = 20.000214$ d from Prša et al. (2010), although the trend in the eclipse timing variations suggest a period $\sim$2 seconds longer. The free parameters of the fit to the light curve are $T_t, T_o, a/r_A, p, i,$ and f_B. We compute the fraction of light blocked by one star by the other using computer code of Mandel & Agol (2002). Because the latter code was designed for planetary transits and models the nearer body as an entirely dark and opaque circular disk, we account for the light from the nearer star appropriately by superposition.

We estimate the limb darkening parameters $(u_{1,A}, u_{2,A}) = (0.243, 0.371)$ and $(u_{1,B}, u_{2,B}) = (0.107, 0.350)$ for stars A and B respectively as appropriate for their effective temperatures, gravities, and metalicities (Table 2). For star A, those are estimated from spectroscopy (Section 4.2). For star B, we estimate its effective temperature $T_{eff} = 3390 \pm 50$ K, by interpolating a grid of model atmosphere spectra (Hauschildt et al. 1999[4]) to match the depth of the light curve at secondary eclipse; we integrate the spectra over the Kepler bandpass and compare to that of star A, accounting also for the relative solid angles, k^2. We estimate star B's gravity log(g) = 4.9 in cgs units from its mass $0.28 \pm 0.034\ M_\odot$ and radius $0.34\ \pm 0.013\ R_\odot$. We assume star B's metalicity is equal to that of star A.

We derive the quantity $e(cos\omega)/\sqrt{1-e^2}$ from the phase of the center of the secondary eclipse relative to the center of primary eclipse. For the latter constraint, we used the analytic approximation for the case of inclination $i = 90^\circ$ (Hilditch 2001, Eq. 5.67), and verified that the difference between that approximation and the numerical estimate for $i > 87^\circ$ is negligible (Hilditch Eq. 5.63). Similarly, the quantity $esin\omega$ equals the ratio of the difference to the sum of the durations of secondary and primary eclipses (Hilditch Eq. 5.69). However, because the eclipse durations are much less precisely measured than the centers, we do not explictly constrain $esin\omega$, although it is weakly constrained implicitly in fitting the light curve. Instead, ω is measured better using the radial velocities (Section 4.3).[5]

---

[3] http://keplergo.arc.nasa.gov/CalibrationResponse.shtml

[4] Machine-readable tables are available at http://svo.cab.inta-csic.es/theory/db2vo/index.php .

[5] We have adopted the equations and viewing geometry of Hilditch's textbook, Figure 2.5. Apparently, prior pub-

Given the above constraints from the light curve, fitting the radial velocities depends on only three astrophysical free parameters: the systemic velocity γ, the velocity semi-amplitude k_1, and the longitude of periastron ω. In our analysis, once ω is measured using the radial velocities, the eccentricity e and the time of periastron passage t_{peri} are analytically constrained from the light curve (Hilditch Eqs. 4.10 and 5.67). Similarly, the uncertainties in the parameters e and t_{peri} flow down from the uncertainty in ω determined from the radial velocities.

The planetary transits of star B, if they occur, are undetectable in the Kepler photometry. Because star B contributes only $f_B = 0.00124$ of the flux of the system, and its relative solid angle $k^2 = 0.0426$, the mean surface brightness of star B is 0.029 that of star A, in the Kepler bandpass. Given that the planet blocks $\sim$0.1% of the system's light when transiting star A, we predict only a 30 ppm planetary transit of star B, i.e. undetectable with Kepler's per-cadence RMS noise of 222 ppm. Because CB transit durations can be no longer than half of the orbital period of the EB (Schneider & Chevreton 1990), or 10 days in this case, and even with an idealized 10-day upper-limit on the duration, the 30-ppm transit depth would correspond to $\sim 3\sigma$, and typically not even that, due to long-term intrinsic variations in the system's total light.

To estimate eclipse time variations, ETVs (Figure 7), we empirically determine the best-fitting center time of each primary eclipse individually by simply minimizing χ^2, while adjusting only the center time of the model curve. The model is simply the Mandel & Agol (2002) curve that best-fits the ensemble of primary eclipses, although simpler, non-physical models such as Gaussians or U-shaped curves produce very similar ETVs. We evaluated the statistical significance of the measured ETVs by simulation. We superposed model eclipses upon the detrended Kepler data at random phases far from the actual primary or secondary eclipses, and produced simulated ETVs that are slightly smaller in amplitude than the actual ETVs, implying that the measured ETVs may have a contribution from the gas-giant planet but are essentially consistent with noise (Figure 7).

Figure 13 and 12 are schematic scale drawings of the EB system. Figure 13 illustrates the sizes of the three objects (star A, star B, and the planet) relative to each other and to the barycentric orbit of star A, which stretches only a few stellar radii across. The schematics also illustrate the positions of the stars at the epochs of each of the five planetary transit events. Because we have approximated the transit chord as the diameter of star A for all five planetary transit events, we have not illustrated the orbit of the planet in the schematic diagrams.

In the above analysis, we have assumed that the Kepler photometer records the sum of the light from the two stars. star A and star B, and nothing more, i.e. zero "third light." In our spectroscopic observing, we took care to inspect images from the acquisition cameras, and noted no stars of any

---

lications of CB planets have adopted the opposite viewing geometry, e.g. Fig. 7 of Murray & Correia (2010). This affects ω by 180°.

significance within the range $1-2''$ of KIC 4862625; 2MASS images support this, also. Because poor weather thwarted an attempt at adaptive optics imaging of the environs of KIC 4862625, we were unable to inspect within the $\sim 1''$ seeing limit. In general, however, imaging can never prove there is zero third light, because any system could be a hierarchical triple star. We investigated the effects of assuming a given third-light fraction, f_C = 0, 0.1, and 0.2, of the total light. Table 2 lists the $f_C = 0$ solution: $k = r_B/r_A = 0.212$, $a/r_A = 21.95$, and $i = 87.57^\circ$, and that solution is used throughout the paper. For $f_C = 0.1$ those parameters are $k = r_B/r_A = 0.228$, $a/r_A = 22.31$, and $i = 87.59^\circ$, and for $f_C = 0.2$ they are $k = r_B/r_A = 0.251$, $a/r_A = 23.01$, and $i = 87.66^\circ$. Thus, compared to the nominal $f_C = 0$ solution, non-zero third light implies larger stellar densities and a larger star B relative to star A.

4.2. Spectral analysis

The SOPHIE spectra of KIC 4862625 without background pollution were co-added for spectral analysis. The Hα and Hβ lines were used to determine the effective temperature $T_{\rm eff} = 6200 \pm 150$ K. This estimate was made on each line independently in order to check the consistency of the results. The spectrum lacks prominent spectral features due to its broad lines combined with the low signal-to-noise ratio. This prevents us from carrying out a detailed spectroscopic analysis. We could not derive accurate estimate of the surface gravity from the Mg I triplet and the Na I doublet. The estimation from these lines is $\log g \simeq 4.0 \pm 0.2$; it is a typical value for main sequence and subgiant stars in that $T_{\rm eff}$ range. We do not find any evidence of Lithium in the spectrum nor any sign of chromospheric activity in the Ca II H and K lines, but the Hα core shows some variable emission features. From the width of the CCF we derived $v \sin i_* = 31 \pm 2\,{\rm km\,s^{-1}}$ and [Fe/H] $\simeq -0.15$.

Using these values of $T_{\rm eff}$, $\log g$, and [Fe/H], we estimated the mass and radius of the star by comparison with a grid of STAREVOL stellar evolution models (A. Palacios, priv. com.; Lagarde et al. 2012). We generated a series of Gaussian random realizations of $T_{\rm eff}$, [Fe/H] and $\log g$, and for each realization we determined the best evolutionary track using a χ^2 minimization on these three parameters. We found $M_\star = 1.23 \pm 0.20\,{\rm M}_\odot$, $R_\star = 1.70 \pm 0.25\,{\rm R}_\odot$, and an isochronal age of $2.6^{+3.6}_{-0.3}$ Gyr.

4.3. Orbital solution of the binaries

For each targets, the APO and SOPHIE radial velocities were fit simultaneously with a Keplerian model. The fits are mainly constrained by the SOPHIE data, which are more numerous

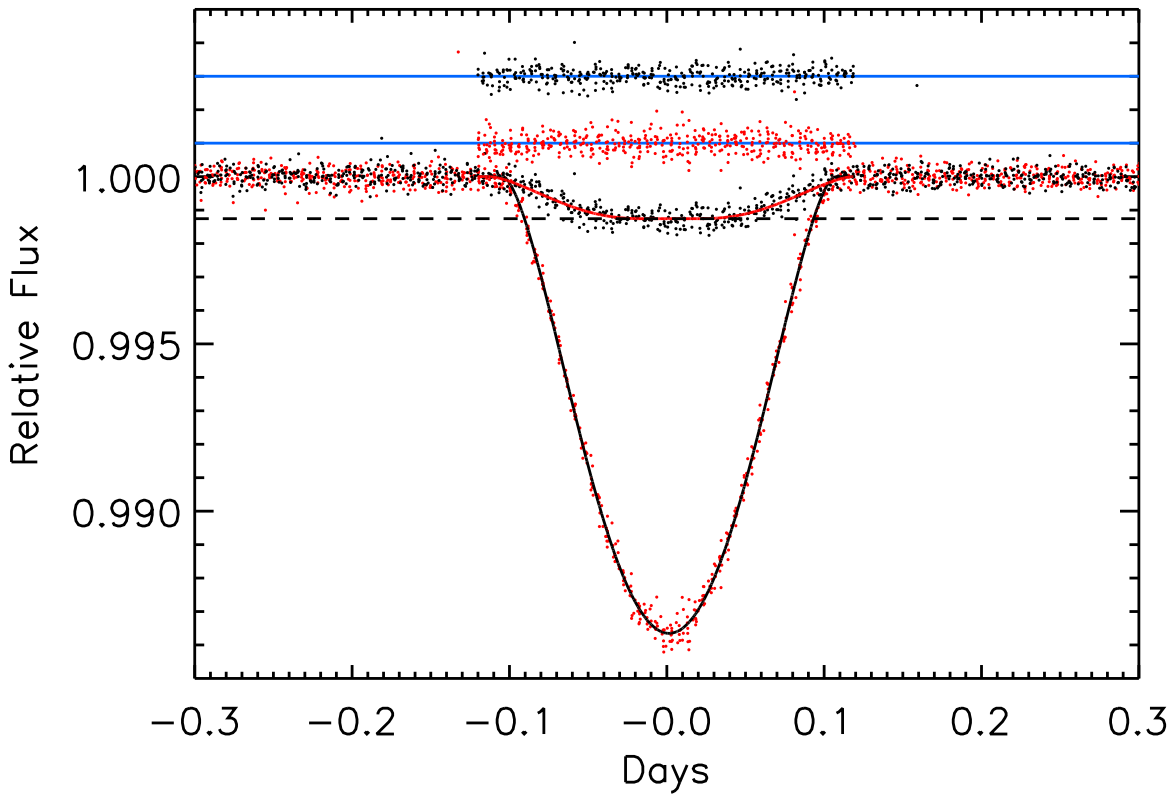

Fig. 6.— Kepler light curves of KIC 4862625. The normalized and detrended flux of the primary and secondary eclipses are shown with respect to the orbital phase of the EB, along with the binary star model. The secondary eclipse data have been centered at zero phase for comparison with the primary eclipse data. The secondary eclipse data and the residuals (above) have been offset vertically for clarity.

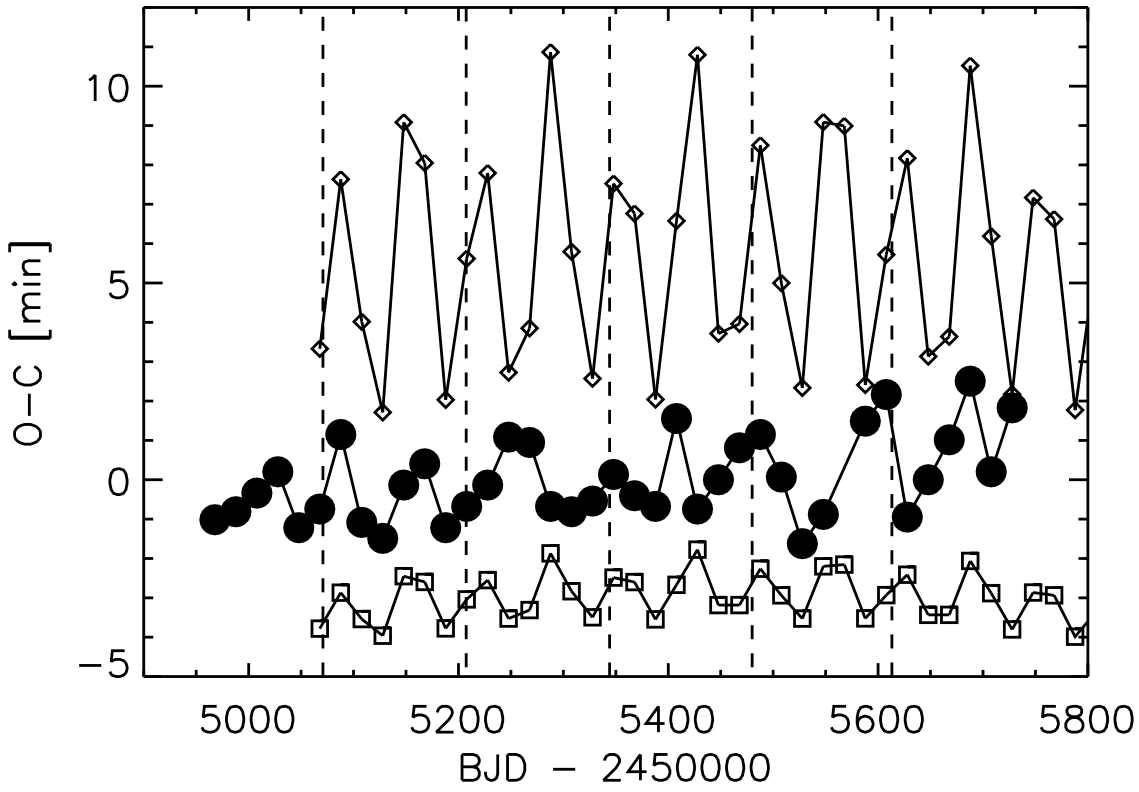

Fig. 7.— Eclipse timing variationsof KIC 4862625. The observed times of each primary eclipse minus the calculated times for a linear ephemeris are shown versus time (an "O-C" diagram). The five planetary transit events are indicated by vertical dashed lines. A single primary eclipse is missing from the sequence at BJD = 2455567.8.

and accurate. The APO radial velocities are much less accurate, but agree with the orbital solution derived from the SOPHIE data.

In addition to the measured radial velocities, the fits take into account the three constraints derived from the Kepler photometry: specifically the orbital period P, and the mid-times of transit and occultation, T_t and T_o. The latter parameters strongly constrain $e(cos\omega)/\sqrt{1-e^2}$ (Section 4.1). The radial velocities confirm the orbital eccentricities and allow e and ω to be measured individually. In comparison to the radial velocity uncertainties, the uncertainties in the three parameters derived from photometry have negligible effects on the final uncertainties of the derived orbit parameters.

The fits to the radial velocites were made using the Levenberg-Marquardt method, and the confidence intervals around the best solutions were determined both from χ^2 variations and Monte Carlo simulations. The histograms of the obtained parameters have a single peak and nice Gaussian-like appearance. The derived values and uncertainties are reported in Table 2; the best fits are over-plotted with the data in Fig. 8.

The semi-amplitude of the radial velocity variations of KIC 4862625 is $K = 18.06 \pm 0.48$ km s^{-1}. With an adopted primary mass $m_A = 1.14 \pm 0.14\,M_\odot$, this translates in a secondary mass of $m_B = 0.28 \pm 0.034$ $M_\odot$. Because KIC 4862625 is single-lined spectroscopic binary, star B's mass depends on star A's and their uncertainties are similarly coupled. For KIC 4862625 the dispersion of the residuals of the fits are 330 m s^{-1} and 3.4 km s^{-1} for SOPHIE and APO data, respectively. The dispersion is similar or even smaller than the expected uncertainties on the measured radial velocities. Uncertainties on the SOPHIE radial velocities might be slightly overestimated. We did not reduce them however in order to be conservative. We cannot detect any significant drift in addition to the reflex motion due to the binaries. For KIC 4862625 we estimate an upper limit ± 10 km s^{-1} yr^{-1} for any additional drift.

Our derived parameters for Kepler-47 agree with those derived by Orosz et al. (2012). The semi-amplitude of the radial velocity variations of Kepler-47 is $K = 31.18 \pm 0.12$ km s^{-1}. With an adopted primary mass from Orosz et al. (2012), $m_A = 1.04 \pm 0.06\,M_\odot$, this translates in a secondary mass of $m_B = 0.357 \pm 0.013\,M_\odot$. Because there are so few RV measurements for Kepler-47, their dispersion is less than the expected measurement uncertainty. For Kepler-47 the dispersion of the residuals of the fits are 25 m s^{-1} and 2.6 km s^{-1} for SOPHIE and APO data, respectively.

4.4. Doppler Boosting

The oscillating radial velocity of the primary star of KIC 4862625 is apparent in the Kepler photometry. Due to Doppler boosting, when the star is moving toward the Earth, its observed flux

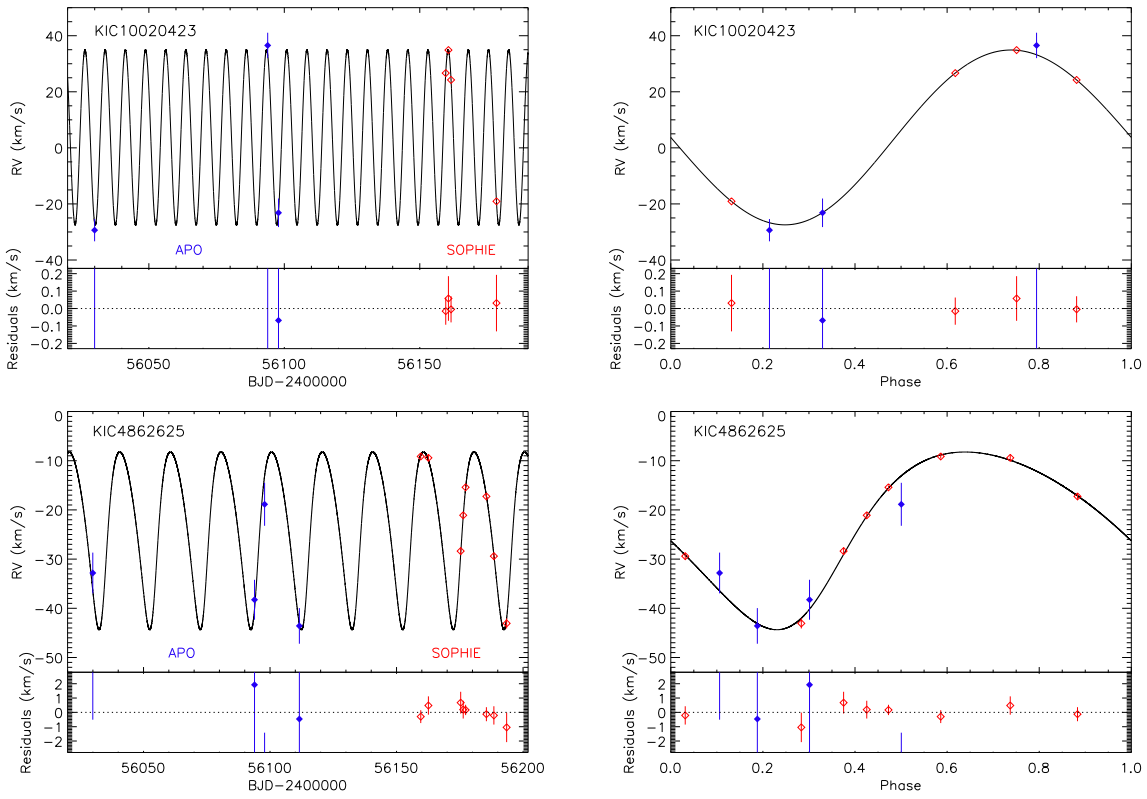

Fig. 8.— Radial velocity measurements of KIC 10020423 (Kepler-47, left) and KIC 4862625 (right) with 1-σ error bars as a function of time (upper) or orbital phase (lower) together with their Keplerian fit and residuals of the fit. The data are from APO (blue, filled diamonds) and SOPHIE (red, empty diamonds).

increases and when the star is moving away, its observed flux decreases. Figure 9 illustrates the modulation in observed flux as a function of the orbital phase of the EB star. To reduce the effect of the rotational modulation on the light curve, we used the mean flux level estimated at each point from the sine wave fit at each point (Section 2.1). We grouped the results in 100 uniformly spaced bins in orbital phase. Hence, each point in Figure 9 represents the median of ~ 350 Kepler measurements. With an RMS of 222 ppm per original Kepler observation, each median would have a formal uncertainty $\sqrt{350}$ less, or 12 ppm if there were no trends in the light curve. However, with the trends, the observed RMS deviation of the medians with respect to the best-fitting boosting curve is 19 ppm.

Due to Doppler boosting, the ratio of observed flux F_λ to emitted flux $F_{0,\lambda}$ is

$$\frac{F_\lambda}{F_{0,\lambda}} = 1 - B\frac{v_r}{c}, \tag{1}$$

where v_r is the stellar radial velocity, c is the speed of light, and the Doppler boosting factor $B = 5 + dlnF_\lambda/dln\lambda$ (Bloemen et al. 2010; Loeb & Gaudi 2003). For a T=6150 K blackbody approximation to the star A's spectrum, and a monochromatic approximation to the Kepler bandpass of $\lambda = 600$ nm, the boosting factor $B_{BB} = 3.99$ (Loeb & Gaudi 2003, Eqs. 2 and 3). At a finer level of approximation, using a template spectrum for an F8 IV star (Pickles 1998) and the Kepler bandpass, we estimate a photon weighted bandpass-integrated boosting factor $B_{F8IV} = 3.73$ (Bloemen et al. 2010, Eq. 3). Both estimates neglect reddening, but its effect is very small for interstellar reddening typical of Kepler stars (Bloemen et al. 2010). Figure 9 compares the Doppler boosting effect estimated with $B = B_{F8IV}$, to the Kepler photometry of KIC 4862625. The boosting factor that best fits the Kepler photometry and the spectroscopic radial velocity curve is $B = 3.46 \pm 0.065$, i.e. or $93 \pm 1.7\%$ of the analytic estimate with $B = B_{F8IV}$. The boosted flux from star B is out of phase with that of star A, but for simplicity of this analysis we have neglected the tiny contribution from star B.

The capability to measure the radial velocity of an EB star using Kepler data alone could be useful and convenient. In principle, CB systems could be "solved" without spectroscopically determined radial velocities. The phase difference of the stellar eclipses constrains well the quantity $ecos(\omega)/\sqrt{1-e^2}$; so the eccentricity e and the longitude of periastron, ω, are constrained by the Kepler photometry. Also, the ratio of the difference in durations (secondary eclipse minus primary eclipse) to the sum of the two durations equals $esin(\omega)$, to a good approximation that the orbital inclination is $\sim 90^\circ$. With Doppler boosting, the Kepler photometry provides the equivalent of a single-lined spectroscopic binary: the radial velocity of the brighter star as a function of orbital phase. The latter also constrains e and ω and the phase of periastron passage, along with a measure of the radial velocity semiamplitude. For stars of similar brightness, the Doppler boosting effects of the two stars will tend to cancel. Of course, the traditional light-curve analysis of the eclipses

provides an estimate of the relative brightnesses of the two stars in an EB. For those eclipsing binaries with one star much brighter than the other, and if that brighter star is photometrically stable or at least predictable as in the case of KIC 4862625's rotational modulation, Doppler boosting curves from Kepler photometry may provide radial velocities adequate for estimating the mass function of the system, and other parameters of the EB.

In this work, we have demonstrated that the stellar radial velocities can be measured either with a spectrometer or a photometer. We give priority to the spectroscopic technique because of its well-calibrated heritage. For comparison we measured $k_1 = 16.7 \pm 0.5$ and $\omega = 222^\circ \pm 2^\circ$ from Doppler boosting in the Kepler light curve. We estimated the maximum-likelihood values of k_1 and ω from all of the photometry. However, because correlations are apparent in the residuals of the Doppler boosting curve, induced by the 2.63-day averaging window during detrending, we estimated the uncertainties of k_1 and ω from subsets of points selected to be independent from each other, in steps of phase equal to 2.63 d / 20 d. The photometrically-determined value of ω is consistent with that determined from shifts of spectral lines, $\omega = 220.2^\circ \pm 3^\circ$. Formally, the photometrically-determined value for ω is more precisely determined than the spectroscopically-determined value. The value of k_1 is prone to systematic error; it is directly proportional to the boost factor B estimated from the overlap integral of the stellar spectrum and the Kepler bandpass. The systemic velocity γ is indeterminate from Doppler boosting.

4.5. Stellar Rotation and Star Spots

From the broadening of the spectral lines and the period of amplitude modulations in the light curve, we infer rotation of star A and determine its radius,

$$R_A = \frac{p_{rot} v \sin i_*}{2\pi\phi}, \tag{2}$$

where ϕ is a factor of order unity that would account for differential rotation and any systematic errors in $v \sin i_*$, such as $\sin i_* < 1$. With $v \sin i_* = 31 \pm 2\,\mathrm{km\,s^{-1}}$, $\mathrm{p_{rot}} = 2.6382 \pm 0.0037$ d, and $\phi = 1$ the stellar radius $R_A = 1.62 \pm 0.1 R_\odot$, in agreement with the estimates from the spectral analysis (Section 4.2) and the photodynamical model (Section 6). With R_A determined from rotation, the density of star A implied from the light curve and the mass function from the radial velocity semiamplitude, we derive a mass $M_A = 1.2 \pm 0.2 M_\odot$, again in agreement with estimates from the other two methods. We also estimated M_A using the predicted velocities of the primary and the planet during the five transits from the best-fit simulations. Each of the five events is scaled for the respective velocities, such that they have approximately the same width. All five are then fit together. The derived parameters of the primary star agree with the above mentioned values within their uncertainties. Because $M \propto R^3$, the fractional uncertainty in stellar mass is three times larger

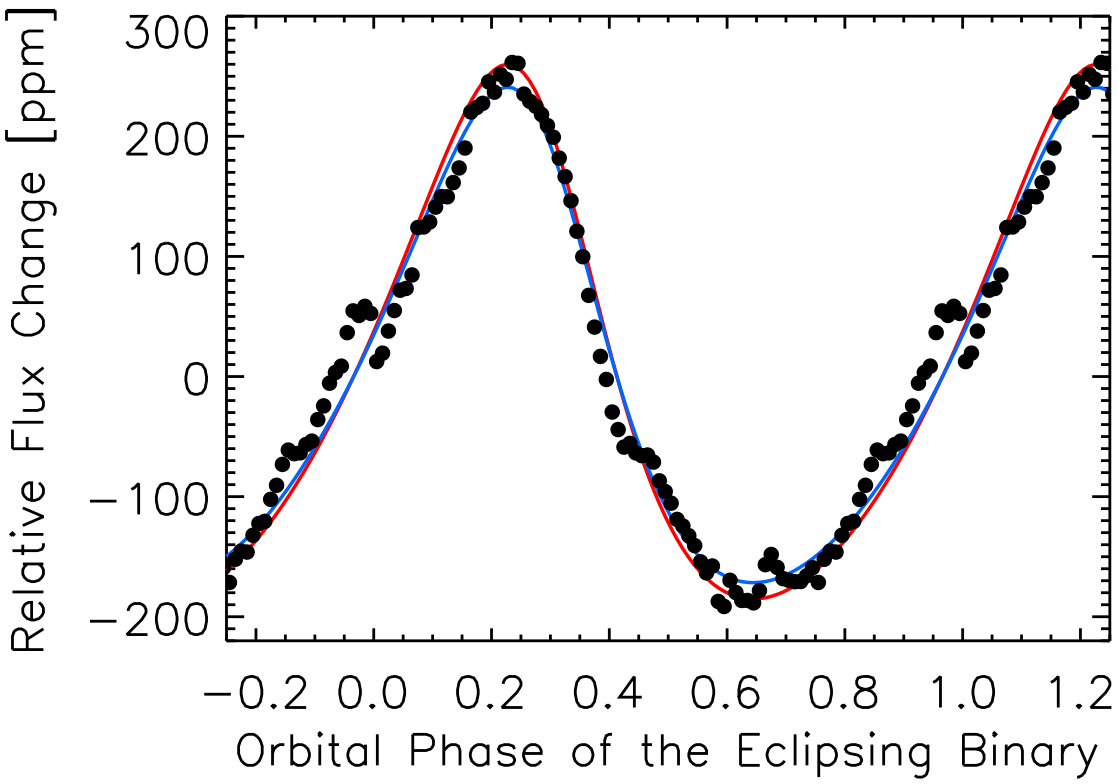

Fig. 9.— Doppler boosting of KIC 4862625. The relative, normalized flux change (see text) is plotted with respect to the EB's orbital phase. The data binned in 0.01 intervals of phase (filled circles) approximately match the flux change estimated from Doppler boosting (red curve) based upon the spectrum of the primary star and its spectroscopically-determined radial velocity curve. The amplitude of the best-fitting curve (blue) is $93 \pm 1.7\%$ that of the estimate (red).

than the stellar radius' fractional uncertainty, which is dominated by the uncertainty in $v \sin i_*$ and any bias implicit in ϕ.

A curious situation is possible with KIC 4862625. Star A's peak orbital velocity transverse to the line of sight is $\sim$18 km s^{-1} and its rotational velocity is 31 km s^{-1} (Section 4.2). Assuming that star A's rotation is prograde with respect to the orbital motions of star B and the planet, and the axis is in the plane of the sky, i.e. sin i = 1, and that the transit is a central one, the transverse velocity of a star spot (or plage) could briefly match that of the planet ($\sim$46 km s^{-1})! Planetary transits could exhibit asymmetric shapes due to the nearly matched transverse speeds. KIC 4862625's transit events 1, 3, and 5 in particular appear asymmetric, with egress being more abrupt than ingress. We are unsure whether the asymmetry is astrophysical or an artifact of the detrending. Because they are grazing, the primary eclipses of KIC 4862625 may not exhibit similar asymmetries if spots (or plage) are not prevalent near the pole of star A, and in any case the projected rotational speeds will be small at the star's poles. Silva (2003, 2008) and Nutzman, Fabrycky, & Fortney (2011) have analyzed star-spot induced asymmetries in transit light curves but did not explicitly consider the possibility of a star spot over-taking a planet. More typically, e.g. for a 3-day period planet transiting a solar-type star rotating every 30 days, the transverse velocity ratio (planet/star) is $\sim$100. Gravity darkening is another mechanism for which very rapid stellar rotation can induce subtle asymmetries in transit light curves (e.g. Barnes, Linscott, and Shporer 2011).

5. Diagnosing a System

Initial diagnosis of a single transiting planet that orbits a stellar binary can be challenging, particularly if orbital period is long and the planet transits only one star. There are many system parameters and potentially only a few observational constraints. In some cases the existing data will not fully constrain the system. Given this potential complexity, it is useful to understand the sequence of analysis steps that build understanding of a newly discovered system. With this in mind, we describe the clues we used to diagnose the KIC 4862625 system.

First, we worried that KIC 4862625 could be an astrophysical false positive. The aperiodicity of the five planetary transits disproves the hypothesis of a background eclipsing binary mimicking a transiting CB planet. Superficially, the false-positive of a dilute EB mimicking planetary transits of a single star (Brown 2003) has an analogy in CB planets, namely that a dilute eclipsing triple star in proximity to an EB star could in principle mimic some of the characteristics of a transiting CB planet. First, however, the chance proximity on the sky of a double star and a triple star will be much rarer than that of a single star and a double star (Lissauer et al. 2012). Second, while one could contrive a dilute triple star to mimic the aperiodic centers of a few transit-like events, the durations in general would not match also, because for a CB planet, the transit durations depend

critically on the characteristics of the EB (Eq. 4). We conclude that a third body orbits the EB star KIC 4862625.

We next analyzed the stellar binary, which has best observational constraints. The Kepler light curve folded on the 20 day period of the stellar binary (Figure 6) has a primary eclipse that is 1.3% deep and a secondary eclipse that is 0.1% deep. Primary eclipses are more V-shaped than U-shaped, suggesting that a smaller secondary grazes a larger primary. Secondary eclipses have a flat bottom with gradual ingress and egress, suggesting that the limb of the primary fully occults the secondary. The phase difference between primary and secondary eclipses indicates an orbit with significant eccentricity.

Next we examine high-resolution spectra of the system. Spectral features are roughly similar to the Sun, except that the lines are shallow and broad. Cross-correlation with a template yields radial velocity shifts consistent with the light curve period of 20 days. Line widths imply $v \sin i_* =$ 31 km s^{-1}, which is typical for spectral types slightly earlier than the Sun. Fitting the measured radial velocities yields eccentricity $e = 0.2$ and semiamplitude $K = 18$ km s^{-1}. The mass function is then 0.008 $M_\odot$, which means $0.23 < M_{\rm sec} < 0.28$ $M_\odot$for $1.0 < M_{\rm pri} < 1.3$ $M_\odot$. As expected, lines of the low-mass secondary are not detected in the optical spectra.

Next we examine the five planetary transits that exist in publicly available Kepler data. First we checked the data quality flags to verify that all data are valid during the transits. Using the PyKE software[6] with custom apertures to analyze Kepler target Pixel files, we confirmed that the five transit events come from the central target pixels. We measured no significant centroid shifts during the transits, which rules out certain astrophysical blending scenarios. We measured transit start and end times by fitting U-shaped functions. We then calculated transit midpoint times and durations.

The cadence and duration of the transits suggest that all involve the primary star. The cadence of the planetary transits yields an apparent orbital period of approximately 136 days. The time differences between successive transits is 136.6, 136.7, 135.9, and 133.2 days. Such regularity is not anticipated for a circumbinary system, where a single object transits or eclipses a "moving target" (Orosz et al. 2012). The regular cadence of transits is not caused simple commensurability, given the 20 and 136 day periods in the system.

We use the durations of the transits to constrain the parameters of the stellar binary. Transit duration depends on chord length and on transverse velocity of the stellar primary relative to the circumbinary object (Schneider & Chevreton (1990). During transits, transverse velocity of the planet is always fairly similar, but transverse velocity of the occulted primary (dependent of the

[6]http://keplergo.arc.nasa.gov/PyKE.shtml

mass ratio of the two stars) changes direction and amplitude throughout its orbit. The amplitude of the transverse velocity of the primary decreases to a minimum at orbital turning points. For eccentric stellar binaries, amplitude also decreases with increasing binary separation. Finally, transit durations are longer when the primary is in the portion of its orbit where transverse velocity of the primary and planet are aligned, and shorter when the two velocities have opposite signs.

With these factors in mind, we now interpret the five observed transits, ordered by increasing duration. Figure 12 illustrates the configuration of the stellar binary at the time of each transit. Transit 2 has the shortest duration because the transverse velocities are oppositely directed and the primary is far from a turning point. Transit 1 has a slightly longer duration because the primary is slowing as it approaches a turning point. Transit 3 is near the other turning point, where binary separation is larger, further reducing relative velocity. Transit 4 has a relatively long duration because the transverse velocities are now aligned, though the primary is near the turning point where binary separation is large. Transit 5 has the longest duration because velocities are still aligned and the primary is near the turning point where binary separation is small. Even longer transit times are possible between points 4 and 5 in Figure 12. Because transit durations are shortest near primary eclipse, the planetary orbit must be prograde relative to the stellar binary.

To quantify constraints provided by observed transit times and durations, we calculated the locations of all bodies in the system as a function of time. Figure 12 shows the view perpendicular to the orbital plane, while Figure 13 shows the view from Earth. The primary has a very similar projected position during transits 1 and 5. Because of this near coincidence, the time difference between transit 1 and 5 is almost exactly four times the 135.59 day orbital period of the planet.

Next, we inspect event 4, also a relatively long duration event. At the phase of event 4, the primary star is near the opposite turning point of its orbit from events 1 and 5. Note event 2 is near primary eclipse, when the two star's relative motions are relatively fast, and the primary star is traveling right to left, i.e. in the opposite direction to the planet, if in our scenario the planet is traveling in a prograde orbit (left to right in this model). Again, event 2 is deeper than secondary eclipse, and event 2's shape is not a square wave, so we consider event 2 is again a transit of the planet across the primary star.

Transverse velocity of the primary is a function of true anomaly, argument of periastron, and eccentricity. Using the nomenclature of Hilditch (2001), transverse velocity V_x is given by

$$V_x = -(\frac{M_2}{M_{bin}})(\frac{2\pi G M_{bin}}{P_{bin}})^{1/3}\frac{(e\sin\omega+\sin(\theta+\omega))}{(1-e^2)^{1/2}}, \quad (3)$$

where $M_{bin} = M_{\rm pri} + M_{\rm sec}$, θ is true anomaly, ω is the argument of pericenter and e is the eccentricity of the binary star.

Using the formalism of Schneider & Chevreton (1990), and assuming a circular orbit for the planet, we obtain the following expression for transit duration $t_{\rm dur}$

$$t_{dur} = \frac{AB}{1+ACx} \tag{4}$$

where

$$\begin{aligned} A &= (M_{bin})^{-1/3} \\ B &= 2R_c(\frac{P_p}{2\pi G})^{1/3} \\ C &= -f(m)(\frac{P_p}{P_{bin}})^{1/3}(1-e^2)^{-1/2} \\ x &= (e\sin\omega + \sin(\theta+\omega)) \end{aligned} \tag{5}$$

In Eq. 5, we use the mass function $f(m)$ obtained from radial velocities to substitute secondary mass (M_2) for binary mass ($M_{\rm bin}$). The mean period of the planet (P_p) is known from the cadence of transit times. Assuming transit chord (R_c) is the same for every transit, we use amoeba/curvefit to fit for the coefficients A and B (C is known to the precision of P_p). The inferred value of parameter B in Eq. 4 constrains stellar radius. Long duration transits will deviate slightly from Eq. 4, if velocity of the stellar primary changes significantly during the transit. We caution that very small changes in observed transit durations can have significant effects on parameters derived from A and B.

To validate Eq. 4, we fitted observed transit durations for Kepler-47b, using transit parameters in Orosz et al. (2012). The fit shown in Figure 10 yields $M_{bin} = 1.35\ M_\odot$and $R_{\rm pri} = 0.87\ R_\odot$, which agrees fairly well with 1.4 $M_\odot$ and 0.96 $R_\odot$ deduced by Orosz et al. (2012). Figure 11 shows an analogous fit for KIC 4862625. We obtain an $M_{bin} = 1.34\ M_\odot$ and $R_{\rm pri} = 1.8\ R_\odot$. The analytic curve indicates that future transits may be as long as a day! To assess uncertainties, we created simulated observations for a mock system like KIC 4862625 (Model 1 in Section 6). We integrated the mock system for 9 planetary orbits, using a time-step of 14.4 min. Blue diamonds in Figure 11 show the result. As with Kepler-47b, the inferred binary mass of 1.35 $M_\odot$ is $\sim$ 8% larger than the expected value of 1.26 $M_\odot$. The chord length calculated from A is 1.9 $R_\odot$, compared to the input value of 1.8 $R_\odot$. The fits to the planetary transit durations using the analytic functions provide a good starting point for the more refined fits presented in Section 6.

In the existing data, depths of the five observed transits appear to change with time. Perhaps this is simply an artifact of our detrending procedure. Alternatively, star spots that perturb the light curve may also affect apparent transit depth. Finally, changes in transit depth could be a manifestation of a planetary orbit with an inclination smaller than 90 degrees.

Numerically integrating an inclined planetary orbit forward in time, the transits fade away, cease for a period, and then return after a large number of orbits. The larger the inclination, the faster the evolution. Given that we have only observed 5 transits so far, we assume that the chord lengths, transit depths, and planetary inclination are constant.

For completeness, we note that the observed dependence of the durations of the five transits on the phase of the binary rule out a retrograde orbit for the planet. Such an orbit should exhibit an opposite trend in a duration versus phase diagram, namely short durations near secondary eclipse and longer ones close to primary eclipses.

6. Planetary Transits

6.1. Methodology

Combined light curve and radial velocity measurements of a circumbinary planet can be characterized by 17 parameters: five orbital elements of the binary (a_{bin}, e_{bin}, ω, Ω, i), six osculating orbital elements of the planet (a_3, e_3, i_3, ω_3, Ω_3, ϕ_0), three masses ($M_{\rm pri}$, $M_{\rm sec}$, m_3), and three radii ($R_{\rm pri}$, $R_{\rm sec}$, r_3). Exhaustively searching a space with 17 dimensions and nonlinear parameters is impractical, so we make simplifying assumptions that allow us to obtain a reasonable solution. As discussed in Section RV, radial velocity measurements yield e, ω, and the stellar mass ratio. The precise Kepler light curve yields the ratio of stellar radii, which depends on derived impact parameters for eclipses that may be grazing. We assume the five observed transits all occult the primary star, so radius of the secondary star drops out of the system. For simplicity, we assume that the planet has negligible mass and orbits in the plane of the sky ($i_3 = 90$ deg). The former assumption is based on the measured ETVs, discussed in Section ETV and expanded below. The latter relies on the hypothesis that the inclination of the planet should be certainly larger than that of the binary for otherwise it would not be seen in transit.

With these approximations, the four remaining free parameters are $M_{\rm pri}$, a_3, e_3, and ω_3. Finding optimal values for these four parameters still requires a very fine numerical grid. For example, a 1% change in mass of the primary star, or in the semi-major axis of the planet can dramatically change the dynamical evolution of the planet, affecting arrival times of observed transits by hours or even days. Arrival times would also be affected if the planet is massive, rather than a massless test particle.

Transit durations (shown in Table 4 have formal uncertainties that do not necessarily account for astrophysical variations in the light curve. To assess how sensitive binary mass is to individual transit durations, we generated and analyzed a set of perturbed observations. We scrambled the five observed transit durations and added a normally distributed perturbation with a standard deviation

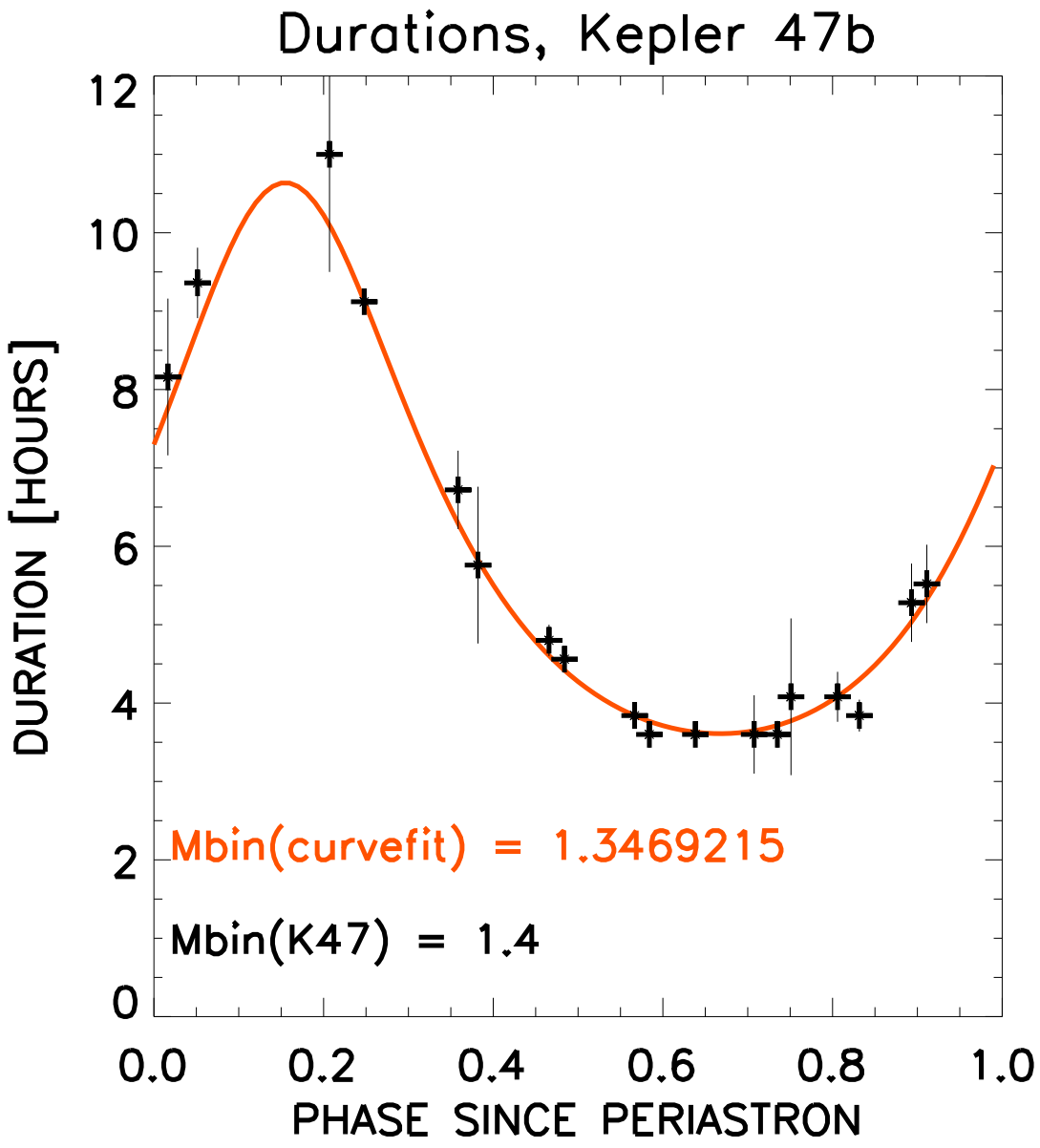

Fig. 10.— Duration versus phase for the Kepler-47b transits. The red curve represents a fit from Eq. 4. The analytic expression recovers the parameters of the binary star very well – $M_{bin,calc} = 1.34 M_{\odot}$ vs $1.4 M_{\odot}$ and $R_{prim} = 0.87 R_{\odot}$ vs $0.96 R_{\odot}$ respectively, provided by Orosz et al. 2012.

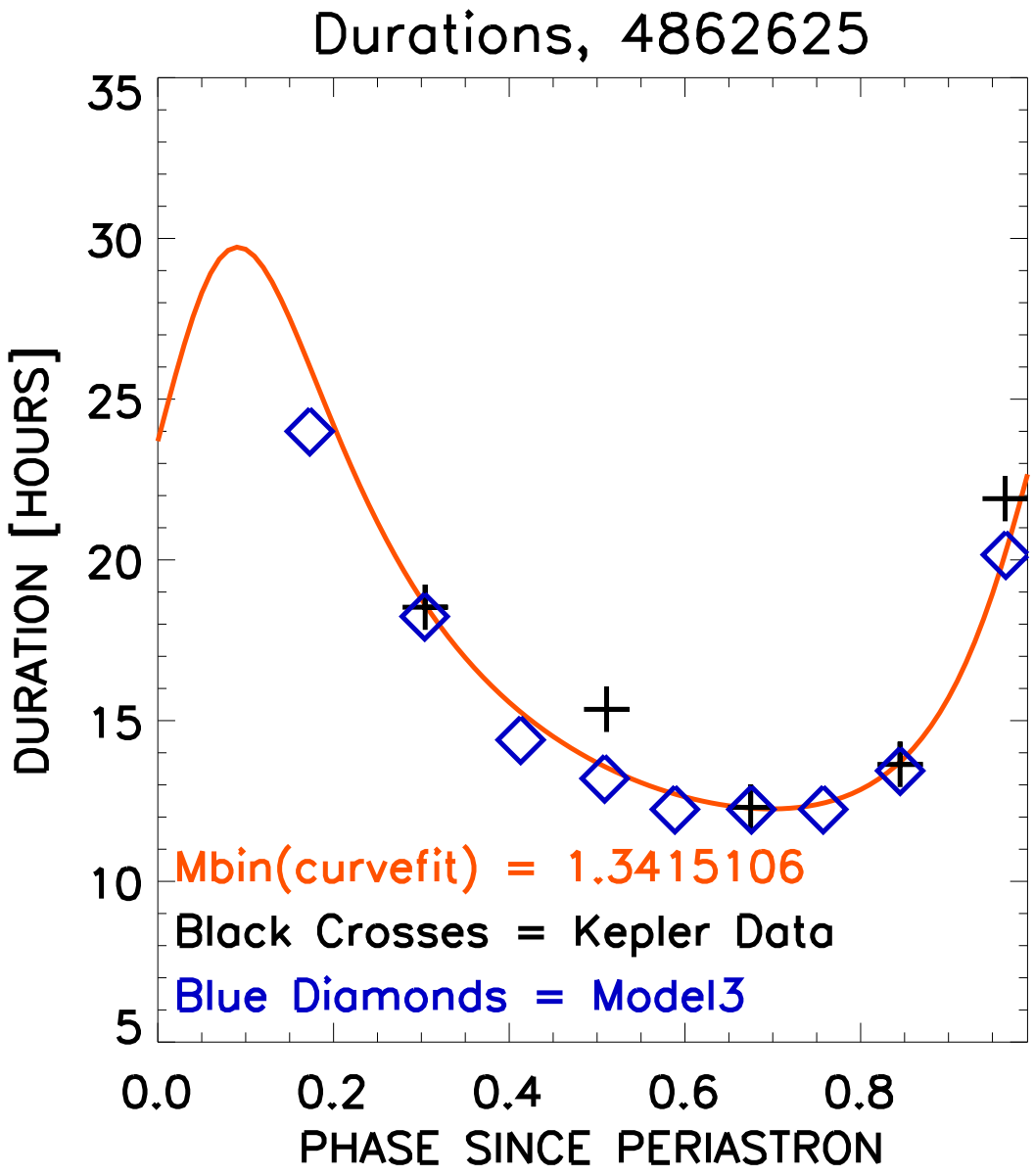

Fig. 11.— Similar to the previous figure but for KIC 4862625. The blue diamonds represent the predicted transits from the dynamical model (Model 1, Section 6). The fit is over the data points, not over the simulated durations, which are shorter than the observed ones by up to an hour (see Table 4). The uncertainties in the measured durations are smaller than the size of the data points.

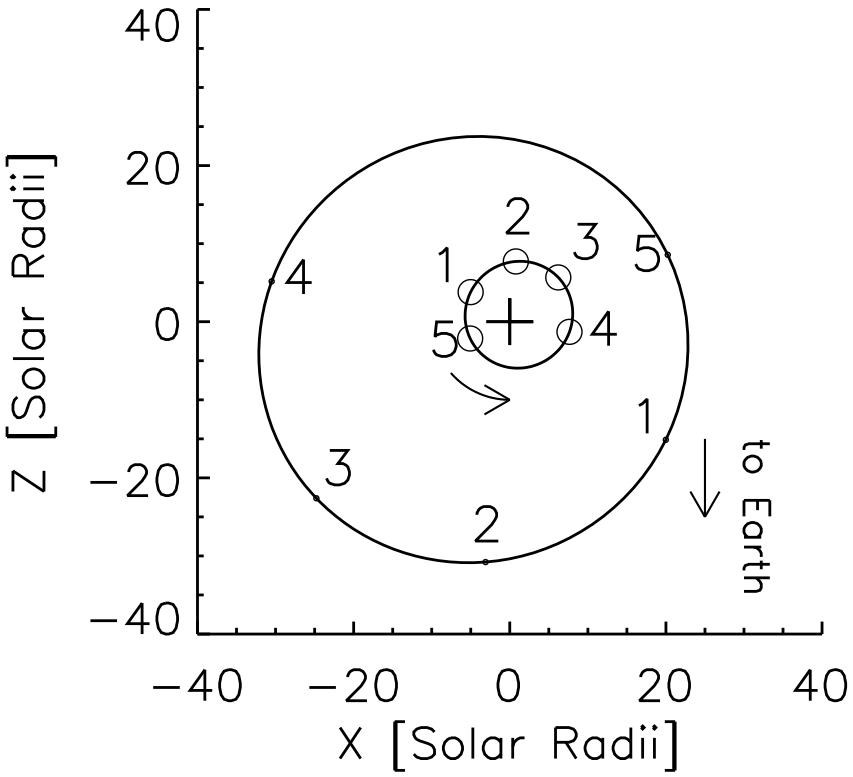

Fig. 12.— Scaled view of the binary system of KIC 4862625 viewed perpendicular the orbital plane. The inner ellipse shows motion of the primary, while the outer ellipse shows the secondary. Numbers along the orbits indicate times of the three transits. The diagram is to scale.

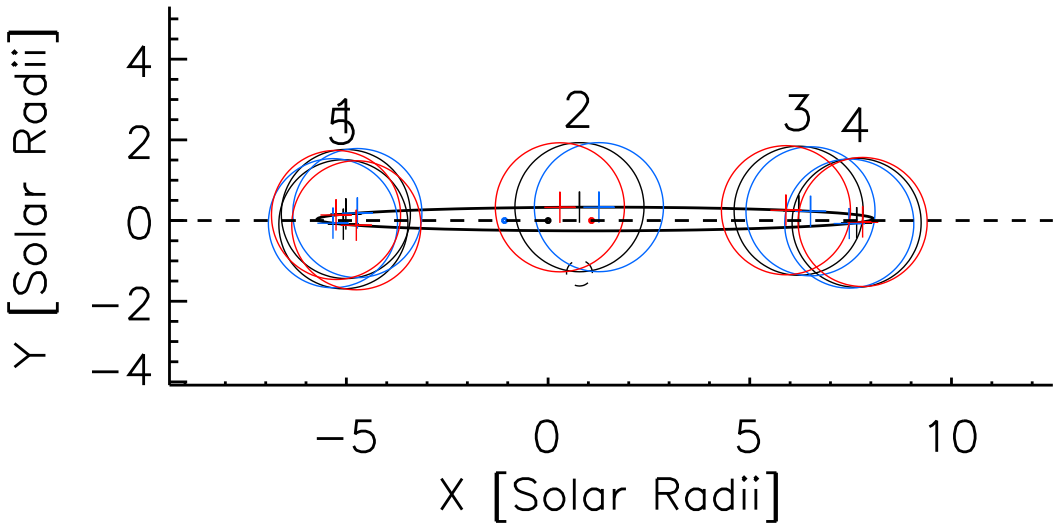

Fig. 13.— Schematic scale diagram of KIC 4862625. The diagram is to scale, with solar radii indicated on the axes. The positions of star A in its orbit (black ellipse) are plotted at the times of the five planetary transits (labeled, black circles centered on black + symbols). The corresponding positions 0.25-day before (blue) and after (red) are also shown, to illustrate the projected velocity of the star. Star B is shown to scale (dashed circle, arbitrarily positioned below star A at event 2). The planet also is shown to scale (smallest circles); again, blue and red correspond to positions −0.25-d and +0.25-d with respect to the position shown in black, which has been arbitrarily centered at the origin.

of 1 hour. We then used Eq. 4 to evaluate the binary mass, obtaining the results shown in Figure 14. Except for a few realizations with unrealistically large perturbations, binary mass is concentrated, with 68% of the values in the range 0.8 to 1.7 $M_{\odot}$. In subsequent analysis, we constrain binary mass to be in this range.

A simple Keplerian solution cannot reproduce observed planetary transit times because the central potential varies as stars in the binary orbit each other. Instead we use a three-body numerical integrator with hierarchical Jacobian coordinates, as will be further described in Section 7. We specify initial conditions (and reference epoch) with respect to the midpoint of the first transit, an arbitrary yet convenient definition. The coordinates of the three bodies are defined with respect to the barycenter of system, which is the barycenter of the stellar binary when planet mass is negligible. We use time-dependent, osculating Keplerian elements to calculate a_3, e_3, i_3, and ω_3 (Doyle et al. (2011)). We use the numerical integrator to compute spatial coordinates for the two stars and the planet. Transits intervals occur when the projected distance between the primary star and planet centers is less than the sum of their radii. Note that parameters cited in this section are instantaneous values for the reference epoch.

First, we used a coarse time step (one third the shortest transit time) to calculate dynamical solutions and corresponding transit midpoint times for a grid of parameter values. The grid step sizes were 0.01 $M_{\odot}$ for $M_{\rm pri}$, 1 $R_{\odot}$ for a_3, and 5 deg for ω_3. Changes of 1 $R_{\odot}$ in a_3 cause significant changes in transit midpoint times. Parameter ranges in the coarse grid were 0.8 to 1.7 $M_{\odot}$ for $M_{\rm pri}$, 0 to 0.2 for e_3, and 0 to 360 deg for ω_3. Next, we used a fine time step (0.01 days) to calculate dynamical solutions for a much finer grid of parameters around the best solutions in the coarse grid. The fine grid includes r_1 as a fifth parameter and calculates transit durations in addition to transit midpoint times. Comparing computed and observed midpoint times and durations for the five transits yields a set of plausible models.

6.2. Results

Even searching in a restricted parameter space, we found multiple solutions that are consistent with the five planetary transit observations. We adopted a goodness of fit metric that is the root mean square (RMS) of observed minus calculated (O−C) midpoint times for transits 2 through 5. The midpoint time for transit 1 always has zero residual because it defines the zero point of time in our calculations. Figure 15 shows goodness of fit for every dynamical model in the grid that matches observed transit midpoint times to better than a RMS of $\sim$ 7 hours. Each point in the figure represents a unique combination of $M_{\rm pri}$, a_3, e_3, and ω_3. Despite a uniformly sampled grid, the number of solutions better than RMS of $\sim$ 7 hours decreases with increasing $M_{\rm pri}$, suggesting that lower $M_{\rm pri}$ is more likely. We note, however, that even though almost half of all solutions fall

within $M_{\rm pri}$between 0.8 $M_\odot$and 0.9 $M_\odot$, most of them have high RMS and are not very likely.

Within the limitations of our grid space search, three solutions stand out from the rest as having an RMS O−C midpoint times of events 2 through 5 to within 1 hour. Granted we may have fallen prey to a local minimum, the three models, labeled M1, M2, and M3 in Figure 15, reproduce the observed planetary transits equivalently well, with a RMS of $\sim$ 1 hour. Further supporting the existence of *a* solution around this particular parameter island stems from them having very similar parameters – all three indicate a primary star of $M_{\rm pri} \sim 1 M_\odot$ (within 1σ of the estimates from the mass function and the spectra) and a planetary orbit with a semi-major axis $a_3 \sim 0.57$ AU, and $e_3 \sim 0.1$. Combined with observational constraints described in previous sections, this implies $M_{\rm sec} \sim 0.26 M_\odot$, $R_{\rm pri} \sim 1.6 R_\odot$ (consistent with our estimates from the spectra and the stellar rotation), $R_{\rm sec} \sim 0.34 R_\odot$, and $P_3 \sim 138$ days. Table 3 gives the best-fit parameters for each solution. The models reproduce well the observed phase-dependance of the durations, with event 2 predicted to be shortest and event 5 – longest. The five observed transits are not sufficient to rule out any of these plausible solutions. Other equivalent or even better solutions may exist, given the coarseness of our initial grid search. We were unable to match observations with a circular orbit ($e_3 = 0$), which is not surprising given that orbital elements evolve continuously. An orbit that is initially circular with change with time, especially when the planet is relatively close to the stellar binary (e.g., KIC 4862625).

To estimate the uncertainty of the derived $M_{\rm pri}$, we examined the distribution of solutions as a function of $M_{\rm pri}$ that have an RMS of less than 3 hours ($\sim 2\sigma$ above the best-fit value). Of the 499 solutions on Figure 14, only 167 comply with this merit criteria, of which 63 fall within $M_{\rm pri}$ between $0.9 M_\odot$ and $1.1 M_\odot$. The distribution is double-peaked with a taller one centered on $M_{\rm pri} \sim 0.8 M_\odot$ and another, smaller peak near $M_{\rm pri} \sim 1 M_\odot$. As mentioned above, the low-mass solutions have significant RMS and, as discussed in Section 4.2, we expect $M_{\rm pri}$ to be $\sim 1 M_\odot$. Thus, we focus on the $M_{\rm pri} \sim 1 M_\odot$ peak, where half of the solutions fall within a range of $M_{\rm pri}$ between $0.9 M_\odot$ and $1.1 M_\odot$, the uncertainty value we adopt under the low-number statistic situation we face. The same approach help us constrain the semi-major axis of the planet and the eccentricity of the orbit but not the argument of periastron where the best-fit values were uniformly spread. We report the values in Table 3.

After global minimization, individual transits should be inspected for significant inconsistencies between observed and model light curves. To illustrate this, Figures 16, 17, and 18 compare our three best models with the five observed transits. Dashed lines indicate observed times of first contact, transit midpoint, and fourth contact. Agreement is very good for all three models, but there are subtle differences – the solutions oscillate around the observed transits. For example, for Model 1 (blue) transit 2 is late, transit 3 is early, and transit 4 is on time. In contrast, for Model 2 (red) transit 2 is on time, transit 3 is on time, and transit 4 is late. It is not obvious which model

is better. The fit is limited by uncertainties in the observed transit midpoint time and resolution of the dynamical models.

To study whether future transits can help break this degeneracy, we continued integrating the three models into the future. Table 4 gives the results, listing midpoint times and durations for future transits 6 through 9. By transit 9 on day 6157 (BJD−2450000), Models 1 and 2 predict transits times that differ by ~ 3.5 hours, which is certainly detectable. Coincidentally, transit 9 will have a long duration and be near the peak of the analytic function described in Section 5, yielding an improved stellar mass constraint. Events 6, 7, and 8 will have short duration and be in the "valley" of the duration curve (Figure 11), providing limited additional information about stellar masses. We note that Figure 15 may be rearranged with the addition of future transits such that our best-fit solutions fall out of grace only to be replaced by other – for example, nearly 50 more solutions are currently within $\sim 2\sigma$ of the best RMS.

We also investigated how non-zero planet mass (1 to 10 M_J) affects transit midpoint time and the precise cadence of stellar eclipses by perturbing Model 1. Using the formalism of Borkovits et al. (2012), we estimate that light travel time effects due to a 10 M_J planet would produce timing changes of only a few seconds. On the other hand, dominant three-body dynamical interactions would produce an amplitude of ~ 5 minutes, which is twice the observed value (Figure 7). Thus, the mass of a coplanar planet should not exceed ~ 5 M_J. We rule out a more massive body on a highly inclined orbit because we observe planetary transits. Figure 19 shows how predicted transit midpoint times change as planet mass increases from 0 to 5 M_J. A large planet tends to arrive earlier for events 2 and 3 and late for 4 and 5, where the deviations are more pronounced for the latter two. We tested several other models and found they all show similar behavior, indicating that while Saturn-mass planets and smaller can be safely approximated as test particles for dynamical purposes, exo-Jupiters' masses need to be properly accounted for in numerical integrations.

6.3. Search for additional transits

We visually examined the light curve of KIC 4862625 for evidence of additional transits. Despite significant variability, there are a few features that are reminiscent of shallow planetary transits. For these features, data flags are normal and centroids have no significant shifts. Some of these extra features occur close in time to the five main transits, most notably around day 5615 (BJD-2450000) when the dynamical model predicts the planet is near the secondary star, but also near days 5045 and 5069, where the two are distinctly apart. The small size and faintness of the secondary, however, means we do not expect to see a quaternary transit (see Section 4.1). Others (near days 5258, 5269, 5298, 5312, 5415; BJD-2450000) cannot be easily associated with the circumbinary planet KIC 4862625b.

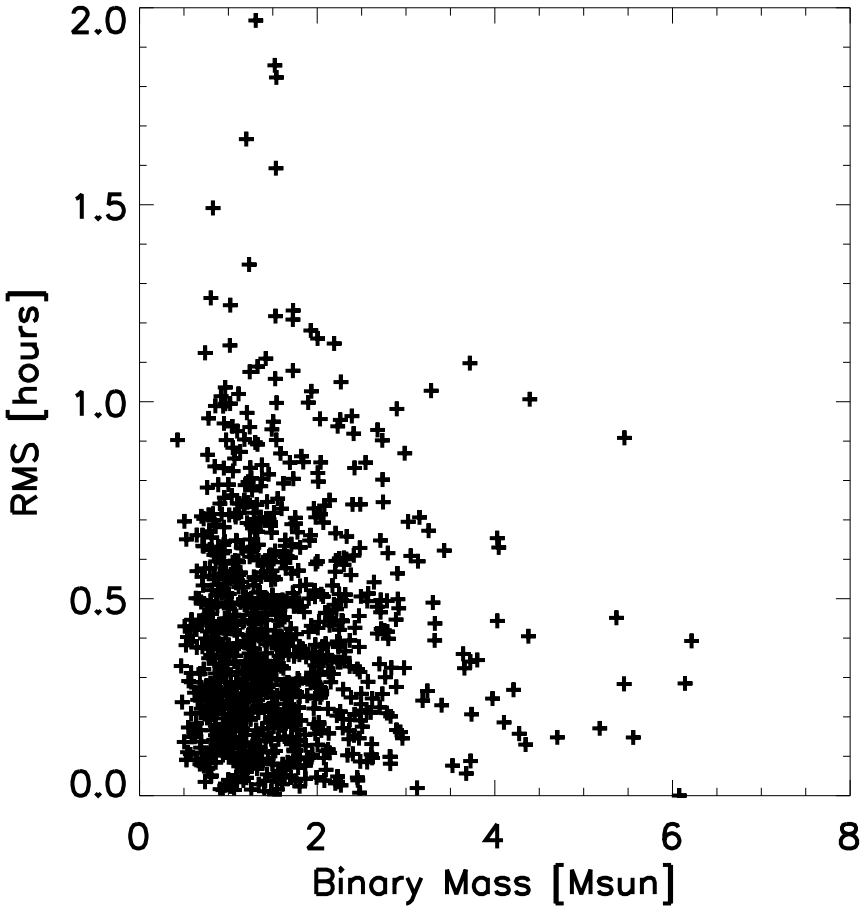

Fig. 14.— Mass of the binary ($M_A + M_B$) derived using the results from the RV measurements and applying Eq. 4 to a thousand iterations of the five planetary transit durations, scrambled and with added normalized noise with σ = 1 hour. 68% of the points fall within binary mass between 0.8 and 1.7 $M_\odot$, providing a manageable search space for the primary mass in our dynamical model of KIC 4862625.

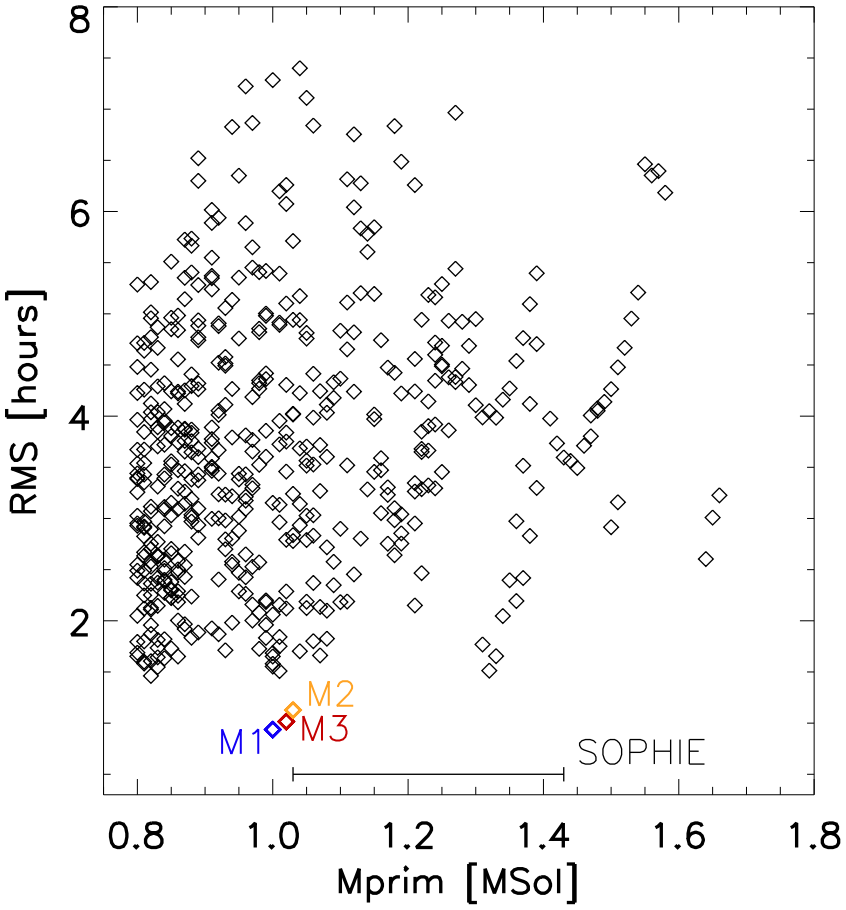

Fig. 15.— Best-fit dynamical models of KIC 4862625 predicting the midpoint times of transits 2 through 5 within an RMS of ~ 7 hours. Models with different parameters produce similar solutions, all predicting planetary transits that deviate by only a few data points from the observed values, a small error margin on the orbital scale of the planet. The decrease in the number of "hits" as the mass of the primary increases from 0.8 to 1.6 is not a systematic effect but is in fact real – there are many more good "hits" for smaller M_{prim}.

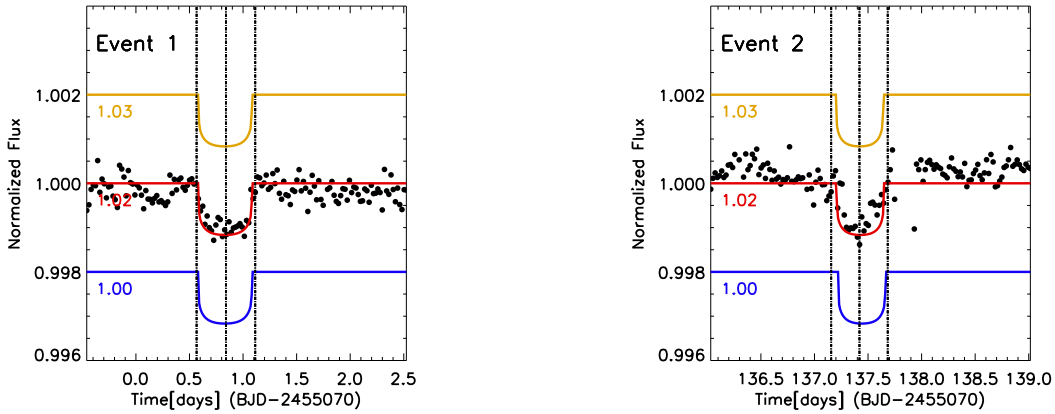

Fig. 16.— The three best-fit dynamical models of KIC 4862625 predicting the midpoint times for transits 1 and 2 to within two hours. The dashed vertical lines define the time of first contact, midtransit time and time of fourth contact, from left to right respectively. All three models are consistent with a primary star of $1.6R_{\odot}$ radius. While the three models predict similar times of transits for events 2 through 5, the differences between them are subtle – the solutions "oscillate" from one event to another. Future events will allow us to further constrain the characteristics of the system. The parameters of the system for the three models are outlined in Table 9.

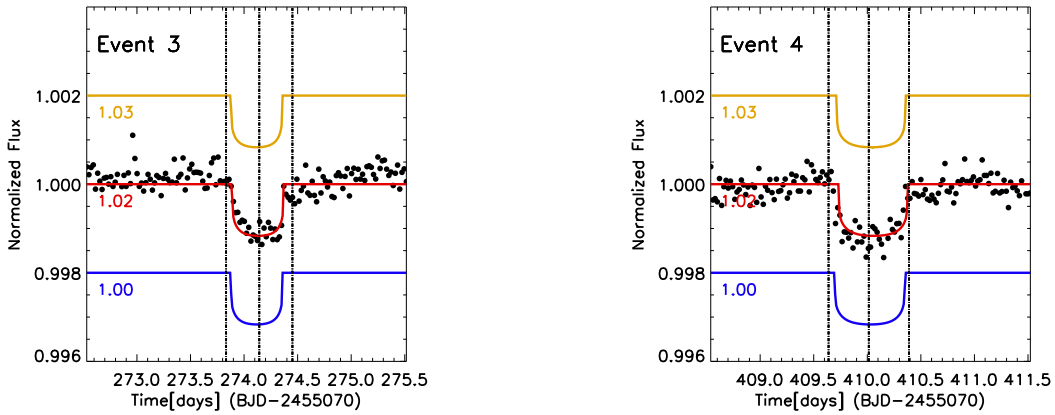

Fig. 17.— The same as the previous figure but for the third and fourth transits of KIC 4862625.

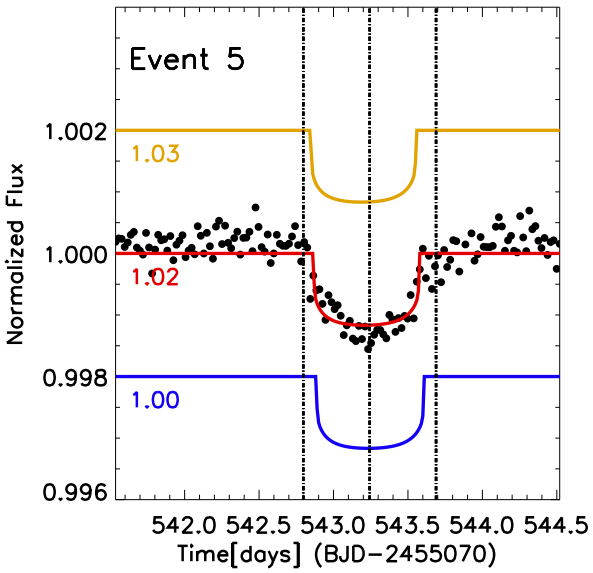

Fig. 18.— The same as the previous figure but for the fifth transits of KIC 4862625.

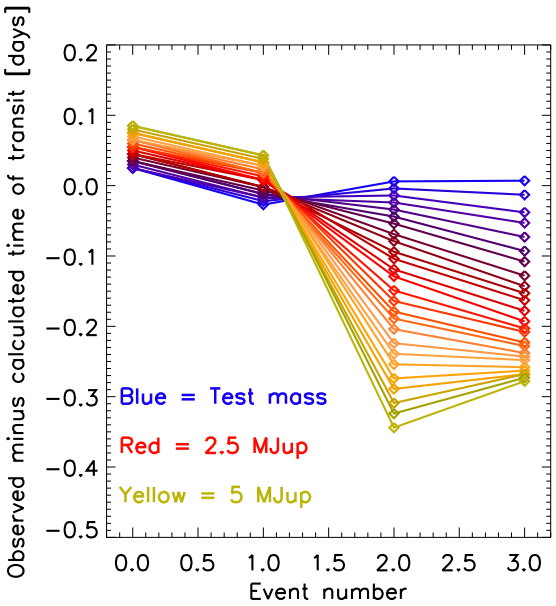

Fig. 19.— The effect of a non-zero planetary mass on the predicted times of transit of KIC 4862625. For the same parameters of the system (Model 1), a increasingly more massive planet introduces significant deviations relative to the best solutions for a massless planet. While it is unlikely that the mass of the planet is larger than a few M_J, it adds a significant complication to the best-fit models, again indicating the non-unique nature of the solutions.

7. Dynamical analysis and orbit stability

We have carried out a dynamical analysis of the KIC4862625 system within the framework of the three-body problem. Such a dynamical system is well known to possibly exhibit complex dynamical behavior. In particular we have carried out a dynamical analysis of the planet around the binary pair in order to detect chaotic regions, often associated with mean-motion resonances (MMRs), in the orbital parameter space of the planet.

We have applied the MEGNO[7] factor (Cincotta & Simó 2002a,b; Cincotta, Giordano & Simó 2003). This numerical technique is efficient in distinguishing between chaotic and quasi-periodic and has found widespread application within dynamical astronomy and the dynamics of multi-body extrasolar planets (Goździewski et al. 2001, 2008; Hinse et al. 2010).

Chaotic orbits are usually (but not always) attributed to unstable orbits. For a quasi-periodic time evolution of the system the dynamics is regular and characterized by only a few fundamental frequencies often associated with stable orbits. However, in order to be precise, quasi-periodic/stable orbits can only be quoted as stable up to the considered integration time. Knowledge on the subsequent dynamical evolution of the system is still hidden to the experimenter. In this work we have experimented with various integration length and found an integration time scale that is long enough to detect the most important mean-motion resonances close to the osculating orbital elements of the transiting planet KIC4862625b.

For reasons of optimization and execution speed we applied the most recent implementation of the MEGNO technique using Poincaré variables (Goździewski 2003; Goździewski et al. 2008). In this reference frame the coordinates of each body are expressed in an astrocentric frame with the most massive object at rest and velocities are relative to the systems barycenter. We use geometric Jacobian coordinates as our initial conditions where the planets orbital elements are relative to the barycenter of the binary system. The Jacobian cartesian coordinates are then transformed to Poincare elements. The numerical integration of the equations of motion and the corresponding variational equations (Mikkola & Innanen 1999) are based on the ODEX[8] integration algorithm (Hairer et al. 1993).

To compute MEGNO maps we used the MECHANIC[9] software (Słonina, Goździewski & Migaszewski 2012; Słonina et al. 2012) which utilizes a Message Passing Interface (MPI) based framework that implements massive single serial dynamical problems for parallel execution in a multi-processor

[7]Mean Exponential Growth of Nearby Orbits

[8]http://www.unige.ch/math/folks/hairer/

[9]http://git.astri.umk.pl/projects/mechanic.

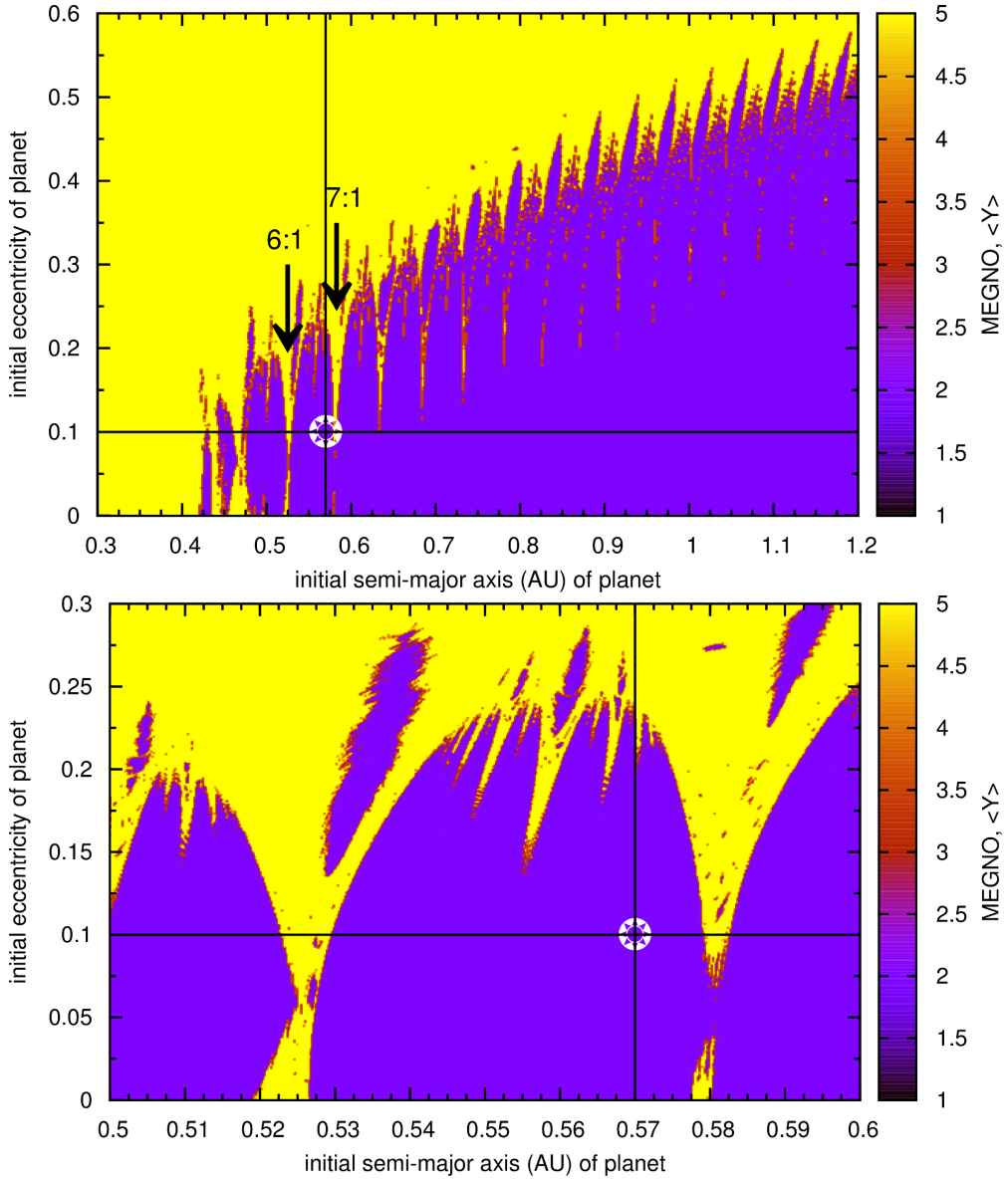

Fig. 20.— Upper panel: MEGNO map of KIC 4862625b. The mass of primary and secondary component were set to 1.0, 0.26 $M_{\odot}$, respectively. The binary semi-major axis and eccentricity was set to 0.156 AU and 0.2. The planet was treated as a test particle. The cross-hair marks the best-fit osculating elements $(a,e) = (0.57\ \mathrm{AU}, 0.1)$ of the planet. Arrows indicate the location of mean-motion resonances. Yellow (or light) color denotes chaotic (possibly unstable) orbits and blue (dark) color denotes quasi-periodic orbits with $|\langle Y \rangle - 2.0| \simeq 0.001$. Lower panel: Same as the upper panel but now zooming into a narrower region of (a,e)-space of the planet. *See electronic version for colors.*

computing environment. Usually we allocated 60 CPUs to compute a single dynamical MEGNO map with typical resolution of 500 x 350 initial conditions. Typical integration time of a single orbit covered about 5×10^4 binary orbits ($\simeq$ 2700 years).

When investigating a dynamical system the MEGNO factor (usually denoted as $\langle Y \rangle$) has the following mathematical properties. In general, MEGNO has the parameterization $\langle Y \rangle(t) = \alpha t + \beta$ (see references above). For a quasi-periodic chaotic initial condition, we have $\alpha \simeq 0$ and $\beta \simeq 2.0$ for $t \to \infty$ asymptotically. If the orbit is chaotic, then $\langle Y \rangle \to \lambda t/2$ for $t \to \infty$. Here λ is the maximum Lyapunov exponent of the considered initial condition. In practice, we terminate a given numerical integration of a chaotic orbit when $\langle Y \rangle > 12$. In our MEGNO maps we color code chaotic initial conditions with yellow and quasi-periodic with blue color.

In Fig. 20 we show a MEGNO map displaying the dynamics of a planet in semi-major axis (a) and eccentricity (e) space. The planet was assumed (justified by the planet displaying transit-like signals) to be co-planar with the binary orbit and all planetary orbital angles were set initially to zero. We remind the reader that the shown elements are referred to a Jacobian reference system with the planets semi-major axis being measured relative to the binary barycenter. The secondary binary component was also started with all orbital angles initially set to zero. The mass of the two binary components were set to 1.0 and 0.26 $M_\odot$ for the primary and secondary component respectively. Referring to Fig. 20 we identify the location of several mean-motion resonances in the system appearing as vertical chaotic columns at constant semi-major axis. The derived orbital elements of the circumbinary planet have $(a,e) = (0.57, 0.1)$ placing the planet in a quasi-periodic region between the 6:1 and 7:1 mean-motion resonance. We show a zoom-in plot in the lower panel of Fig. 20. For planetary eccentricities larger than $e \simeq 0.25$ the planets orbital pericenter distance $(q = a(1-e))$ starts to become comparable to the binary separation resulting in close encounters and hence strongly chaotic and most possibly unstable behavior. We detected collisions of the test mass with one of the binary components and/or ejection of the planet from the system by carrying out single orbit integrations of the planetary orbit for eccentricities around 0.25 and higher.

We investigated the significance of the mass parameter of all involved objects on the overall dynamics. We recomputed the map shown in Fig. 20 for various masses of the planet by considering 1 M_{earth}, 10 M_{earth}, 1 M_{jup}, 10 M_{jup} and 50 M_{jup} masses and found no significant qualitative difference in the global dynamics of Fig. 20. From comparison we found that all maps resemble each other more or less qualitatively. In a similar mass parameter survey study we also considered different mass combinations of the binary components that seemed most plausible (see previous sections) and conclude that only small qualitative changes were observed for small changes in the components mass. However, the most significant changes were detected to be close to the location of mean-motion resonances. We note that the timescales of precession frequencies of some of the orbital elements might change significantly for different mass parameters. In addition, we also

note that the ETVs can also change significantly for different masses as discussed earlier.

We conclude this section by noting that the best-fit orbital parameters locates the transiting planet KIC4862625b in a quasi-periodic region in (a, e)-space rendering our solution to be plausible from a dynamical point of view. We point out that our work suggest that the planet is relatively close to the 7:1 mean-motion resonance with the binary. We speculate that future observations will reveal whether the planet is or is not part of a resonant configuration.

8. Discussion

A single transit event indicates the presence of a third body in an eclipsing binary system. Two transits can define an approximate orbital period for the third body, albeit with uncertainties associated with aliasing and data gaps, or orbital inclination that can prevent a planet from transiting the moving targets of the two stars on each passage of the planet. Even with a few planetary transits observed, unraveling the system configuration can be challenging.

In general order of increasing challenge, the system configurations for circumbinary planets can be solved for double-lined, double-dipped circumbinaries (planet transits are detected across both stars, e.g. Kepler 34 and 35), followed by double-lined, single-dipped circumbinaries (planetary transits are detected across only one of the stars) and the single-lined circumbinaries, double-dipped and single-dipped. For double-lined eclipsing binary stars, spectra provide the individual stars' masses; for single-lined eclipsing binaries, spectra provide only the mass function that relates the two masses to each other, not the two masses individually. Transits of a third body can break the latter degeneracy inherent to single-lined systems. Single-lined, double-dipped systems wherein transits across both stars occur during a single binary orbit, allow excellent constraints on the masses of the binary stars, as anticipated by Schneider & Chevreton (1990) and demonstrated for Kepler-16 by Doyle et al. (2011). Whether a binary is single- or double-lined depends on observational capabilities; for example, Kepler-16 was originally a single-lined double-dipped system; it has since changed its category to a double-lined system due to very high sensitivity spectra (Bender et al. 2012). Likewise, whether a system is single- or double-dipped also depends on the observational capabilities: even if a planet transits both stars, we may not be able to discern the transits of the fainter star, e.g. KIC 4862625. More challenging than the systems that are either double-lined or double-dipped are the single-lined and single-dipped circumbinary systems such as Kepler-38, Kepler-47 and KIC 4862625. A large number of planetary transits, as in the case of Kepler-47b, helps photodynamical modeling to constrain system parameters via Eq. 4 (cf. Figure 10). However, if only a few transits occur, e.g. Kepler-38 and KIC 4862625, there may be doubt as to the uniqueness of a solution with a large number of system parameters.

From the broadening of the spectral lines and the period of amplitude modulations in the light curve, we infer rotation of star A and determine its radius, which in combination with $log(g)$ from stellar spectra or the density of star A from the stellar eclipses, either one indicates a Solar-mass primary star. Small- or undetectable deviations from a linear ephemeris in the primary eclipse times prove the planet is of planetary, not stellar, mass.

The five planetary transits further constrain the parameters of the two stars, as their center times and durations depend on the ratio of the stellar masses and on the transiting chord length (Eq. 4). The latter breaks the degeneracy inherent to the mass function of the single-lined spectra. Thereby we constrain the individual stellar masses of of KIC 4862625 and Star A's radius, assuming central planetary transits. Similarly, we confirm the parameters of the Kepler-47 system reported by Orosz et al. (2012).

To solve the dynamical nature of the KIC 4862625 system we did a minimization search over a grid space defined by m_1, a_3, e_3, and ω_3, using a three-body numerical integrator in Jacobian coordinates. Taking the first event as a reference point, we found a set of best-fit solutions, defined by the system parameters of the four-dimensional grid space listed above, that predict the midtransit times and durations of the subsequent four events to within an hour. The simulations match the observed events well but we caution that the combination of fixed grid resolution, triaged parameters space, and the small number of transits limit our ability to choose one of the best fit models over another. Observations of a few additional transits will differentiate our models, because the optimal solutions diverge in their predictions for the center times of the planetary transits.

To detect chaotic solutions in the parameter space, we studied the long term stability of the system using an extensive set of numerical simulations, applying the MEGNO factor. We tested systems with different planetary masses, between 1 M_{earth} and 50 M_{jup}, to evaluate the changes in the dynamical behavior of the three bodies. We do not detect significant difference outside mean motion resonances; a planet starting near a mean-motion resonance, however, exhibits erratic behavior. The ratio of binary star period to the period of the giant planet is, however, not an integer value, giving us confidence that the planet is not on a chaotic orbit. Its orbit is near but beyond the instability region; the ratio of planetary to binary semi-major axis is ~ 3.6, compared to ~ 2.8 of Holman & Wiegert (1999), which is similar to the other Kepler planets and in agreement with theoretical predictions that such configurations should be common.

9. Conclusions

We report the discovery and characterization of a gas giant $r = 0.49 \pm 0.018\, r_{Jupiter}$ circumbinary planet transiting the KIC 4862625 eclipsing binary system. The planet revolves around the

two stars every $\sim$138 days and transits the $1.14 \pm 0.14\,M_{\odot}$ and $1.59 \pm 0.06\,R_{\odot}$ F8 IV subgiant primary. Dynamical models indicate a slightly smaller mass for the primary star ($1M_{\odot}$) but a similar size ($1.6R_{\odot}$), and a 0.56 AU, $e = 0.1$ orbit for the planet. We describe a simple, semi-automatic procedure specifically designed to search for aperiodic transits in the light curves of binary stars. After identifying the transiting signals, we obtained spectra of the two pairs of binary stars, from which we determined the mass function, eccentricity and argument of periapsis for each pair.

We also describe the independent discovery of the Kepler-47bc circumbinary planets by the same method. We discontinued our characterization of that system soon after it was reported by Orosz et al. (2012). Our truncated characterization confirms the parameters they reported.

We coin a phrase to describe circumbinary planetary systems: if planetary transits are detected for only one star, the system is "single-dipped," and for both stars, "double-dipped." We discuss the relative merits of single- or double-lined and single- or double-dipped circumbinary systems.

Periodic variations in the radial velocity of star A measured by Doppler boosting compare favorably with those obtained by the traditional spectroscopic methods (Figure 9). The example of KIC 4862625 demonstrates the potential of the Doppler-boosting technique for reconnaissance of eclipsing binary stars prior to, or in lieu of, obtaining high-resolution spectra of them.

The family portrait of circumbinary planets discovered by the Kepler mission is filling up quickly, with now seven planets reported in less than a year since the first was reported by Doyle et al. (2011). KIC 4862625 joins its peers Kepler 16b, 34b and 35b in the category of gas giant planets and, like Kepler 38b, orbits a binary system that includes an evolved primary star. With the continued operation of the Kepler mission and its exquisite-quality data, we expect the discovery of circumbinary planets to continue and give us a deeper insight into these exciting systems.

The authors gratefully acknowledge everyone who has contributed to the Kepler Mission, which is funded by NASA's Science Mission Directorate. The KIC 4862625 system has been identified and studied independently by Schwamb et al. (2012); we especially acknowledge the collegiality of Meg Schwamb and Debra Fischer. We acknowledge conversations with Josh Carter, Nicolas Crouzet, Selma De Mink, Holland Ford, Danny Lennon, Douglas Long, David Neufeld, Colin Norman, Jerome Orosz, Rachel Osten, M. Słonina, and K. Goździewski.

This research used observations made with 1) the SOPHIE instrument on the 1.93-m telescope at Observatoire de Haute-Provence (CNRS), France, as part of program 12B.PNP.MOUT and 2) the Dual-Imaging Spectrograph on 3.5-m Apache Point Telescope, as part of programs Q2JH01 and Q2JH07. This research made use of the the SIMBAD database, operated at CDS, Strasbourg, France; data products from the Two Micron All Sky Survey (2MASS), the Digitized Sky Survey

(DSS), the NASA exoplanet archive NexSci[10]; the Exoplanet Data Explorer[11] of Wright et al. (2011); source code for transit light curves (Mandel & Agol 2002); an eclipsing binary simulator[12] ; the theoretical models[13] of Hauschildt et al. (1999); a library[14] of stellar spectra of Pickles (1998); SFI/HEA Irish Centre for High-End Computing (ICHEC); PLUTO computing cluster at KASI. V.B.K. and P.R.M. received funding from NASA Origins of Solar Systems grant NNX10AG30G and from HST DD grant 11945. T.C.H acknowledges support by the Korea Research Council for Science and Technology (KRCF) through the Young Scientist Research Fellowship Program grant number 2012-1-410-02. This research was performed in partial fulfillment of the requirements of the PhD of V.B.K. at Johns Hopkins University.

REFERENCES

Baranne, A., Queloz, D., Mayor, M., et al. 1996, A&AS, 119, 373

Barbieri, M., et al. 2007, A&A, 476, L13

Barnes, J. W., Linscott, E., & Shporer, A. 2011, ApJS, 197, 10

Bender, C. F., Mahadevan, S., Deshpande, R., et al. 2012, ApJ, 751, L31

Beuermann, K., Dreizler, S., Hessman, F. V., Deller, J. 2012, A&A, 543, 138

Bloemen, S., Marsh, T. R., Østensen, R. H., et al. 2011, MNRAS, 410, 1787

Bloemen, S., Marsh, T. R., Degroote, P., et al. 2012, MNRAS, 422, 2600

Borkovits, T., Derekas, A., Kiss, L. L. et al. 2012, ArXiv eprints: 2012arXiv1210.1061B

Bouchy, F., Hébrard, G., Udry, S., et al. 2009, A&A, 505, 853

Brown, T. M., Latham, D. W., Everett, M. E., & Esquerdo, G. A. 2011, AJ, 142, 112

Burke, C. J., Gaudi, B. S., DePoy, D. L., & Pogge, R. W. 2006, AJ, 132, 210

[10]http://exoplanetarchive.ipac.caltech.edu

[11]http://exoplanets.org

[12]http://astro.unl.edu/naap/ebs/animations/ebs.html

[13]http://svo.cab.inta-csic.es/theory/db2vo/index.php

[14]http://www.eso.org/sci/observing/tools/standards/IR_spectral_library.html

Cincotta, P. M., Simó, C. 2000, ApJS, 147, 205

Cincotta, P. M., Simó, C. 2000, CMDA, 73, 195

Cincotta, P. M., Giordano, C. M., Simó, C. 2003, Physica D, 182, 151

Claret, A. 2000, A&A, 363, 1081

Demarque, P., Woo, J-H, Kim, Y-C, & Yi, S. K. 2004, ApJS, 155, 667

Dvorak, R. 1982, Oesterreichische Akademie Wissenschaften Mathematisch naturwissenschaftliche Klasse Sitzungsberichte Abteilung, 191, 423

Dvorak, R. 1986, A&A, 167, 379

Goździewski, K., 2003, A&A, 398, 315

Goździewski, K., Bois, E., Maciejewski, A. J., Kiseleva-Eggleton, L., 2001, A&A, 378, 569.

Goździewski, K., Breiter, S., Borczyk, W., 2008, MNRAS, 383, 989

Goździewski, K., et al. 2012, MNRAS, 425, 930

Hairer, E., Norsett, S., & Wanner, G. 1993, Solving ordinary differential equations I, nonstiff problems, 2nd Ed., Springer Series in Computational Mathematics (Springer-Verlag)

Hébrard, G., Bouchy, F., Pont, F., et al. 2008, A&A, 488, 763

Hinse, T. C., Christou, A. A., Alvarellos, J. L. A., Goździewski, K., 2010, MNRAS, 404, 837

Hinse, T. C., Lee, J. W, Goździewski, K., Haghighipour, N., Lee, C.-U., Scullion, E. M., 2012, MNRAS, 420, 3609

Hilditch, R. W. 2001, An Introduction to Close Binary Stars, by R. W. Hilditch, pp. 392. ISBN 0521241065. Cambridge, UK: Cambridge University Press, March 2001.

Holman, M. J., & Wiegert, P. A. 1999, AJ, 117, 621

Horner, J., Marshall, J. P., Wittenmyer, R. A., Tinney, C. G., 2012, MNRAS, 416, 11

Horner, J., Wittenmyer, R. A., Hinse, T. C., Tinney, C. G., MNRAS, 425, 749

Horner, J., Hinse, T. C.,Wittenmyer, R. A., Marshall, J. P., Tinney, C. G., MNRAS(in press), 2012arXiv1209.0608H

Kovács, G., Zucker, S., & Mazeh, T. 2002, A&A, 391, 369

Lagarde, N., Decressin, T., Charbonnel, C., et al. 2012, A&A, 543, A108

Lissauer, J. J., Marcy, G. W., Rowe, J. F., et al. 2012, ApJ, 750, 112

Loeb, A., & Gaudi, B. S. 2003, ApJ, 588, L117

Mandel, K., & Agol, E. 2002, ApJ, 580, L171

Mazeh, T., & Faigler, S. 2010, A&A, 521, L59

Mikkola, S., Innanen, K., 1999, CMDA, 74, 59

Murray, C. D., & Correia, A. C. M. 2011, Exoplanets, edited by S. Seager. Tucson, AZ: University of Arizona Press, 2011, 526 pp. ISBN 978-0-8165-2945-2., p.15-23

Nutzman, P. A., Fabrycky, D. C., & Fortney, J. J. 2011, ApJ, 740, L10

Orosz, J. A., Welsh, W. F., Carter, J. A., et al. 2012, Science, 337, 1511

Orosz, J. A., Welsh, W. F., Carter, J. A., et al.ApJ, 758, 87

Pepe, F., Mayor, M., Galland, F., et al. 2002, A&A, 388, 632

Pickles, A. J. 1998, PASP, 110, 863

Prša, A., Batalha, N., Slawson, R. W., et al. 2011, AJ, 141, 83

Schneider, J., & Chevreton, M. 1990, A&A, 232, 251

Silva, A. V. R. 2003, Bulletin of the Astronomical Society of Brazil, 23, 15

Silva-Valio, A. 2008, ApJ, 683, L179

Slawson, R. W., Prša, A. Welsh, W. F. et al.AJ, 142, 160

Słonina, M., Goździewski, K., Migaszewski, C., Rozenkiewicz, A., 2012, ArXiv eprints: 2012arXiv1205.1341S, submitted to MNRAS

Słonina M., Goździewski K., Migaszewski C., 2012, in F. Arenou & D. Hestroffer ed., Orbital Couples: Pas de Deux in the Solar System and the Milky Way (arXiv:1202.6513v1,in print) Mechanic: a new numerical MPI framework for the dynamical astronomy

van Kerkwijk, M. H., Rappaport, S. A., Breton, R. P., et al. 2010, ApJ, 715, 51

Wright, J. T., Fakhouri, O., Marcy, G. W., et al. 2011, PASP, 123, 412

Table 1: Measured radial velocities.

BJD_{UTC} $-2\,400\,000$	RV ($km\,s^{-1}$)	$\pm1\sigma$ ($km\,s^{-1}$)	Telescope/ Instrument
KIC 4862625			
56 029.9593	−30.3	4.1	APO
56 093.8661	−35.7	4.1	APO
56 097.8526	−16.3	4.4	APO
56 111.6009	−41.0	3.6	APO
56 159.5657	−9.13	0.45	OHP193/SOPHIE
56 162.5848	−9.42	0.64	OHP193/SOPHIE
56 175.3481	−28.37	0.76	OHP193/SOPHIE
56 176.3531	−21.09	0.62	OHP193/SOPHIE
56 177.2970†	−15.41	0.50	OHP193/SOPHIE
56 185.5063	−17.26	0.49	OHP193/SOPHIE
56 188.4707	−29.40	0.64	OHP193/SOPHIE
56 193.5113	−43.07	1.03	OHP193/SOPHIE
KIC 10020423 (Kepler-47)			
56 029.9593	−65.9	4.0	APO
56 093.8661	0.0	4.5	APO
56 097.8526	−59.7	5.1	APO
56 159.5866	26.67	0.08	OHP193/SOPHIE
56 160.5787	34.88	0.13	OHP193/SOPHIE
56 161.5490	24.22	0.08	OHP193/SOPHIE
56 178.3126	−19.07	0.16	OHP193/SOPHIE

†: measurement corrected for sky background pollution.

Table 2: Parameters of the Binary Star Systems.

KIC 4862625					
Parameter	Symbol	Value	Uncertainty (1σ)	Unit	Note
Orbital Period	P	20.000214	-	d	Prša et al. (2011)
Epoch of primary eclipse	$T_{transit}$	2454967.81963	-	BJD	Prša et al. (2011)
Epoch of secondary eclipse	$T_{occultation}$	2454975.6738	0.001	BJD	
Epoch of Periastron passage	T_0	2454973.862	0.15	BJD	
Velocity semi-amplitude	K_1	18.06	0.48	km s^{-1}	
Velocity offset	$\gamma(SOPHIE)$	-23.25	0.26	km s^{-1}	
Velocity offset	$\gamma(APO)$	-20.7	1.8	km s^{-1}	
Argument of Periapsis	ω	220.2	3	°	
Eccentricity	e	0.2207	0.0093		
Semimajor Axis	a	0.1622	0.005	AU	
Orbital Inclination	i	87.572	0.006	°	
Normalized Semimajor Axis	a/r_A	21.95	0.15		
Radius of Star A	r_A	1.59	0.06	$R_\odot$	
Radius of Star B	r_B	0.34	0.013	$R_\odot$	
Ratio of radii	k	0.2122	0.015		$k = r_B/r_A$
Mass of Star A	m_A	1.14	0.14	$M_\odot$	
Mass of Star B	m_B	0.28	0.034	$M_\odot$	
Temperature of Star A	T_A	6200	150	K	
Temperature of Star B	T_B	3390	50	K	
V sin i of Star A	$vsini$	31	2	km s^{-1}	
Fe/H of Star A	$[Fe/H]$	-0.15			
Gravity of Star A	log(g)	4.0	0.2		Spectroscopic
Isochronal age of Star A		2.6	$+3.6/-0.3$	Gyr	
KIC 10020423 (Kepler-47)					
Orbital Period	P	7.44837695	0.00000021	d	Orosz et al. (2012)
Epoch of primary eclipse	$T_{transit}$	2454963.24539	0.000041	BJD	Orosz et al. (2012)
Epoch of secondary eclipse	$T_{occultation}$	2454959.426986	0.000277	BJD	Orosz et al. (2012)
Epoch of Periastron passage	T_0	2454965.792	0.076	BJD	
Velocity semi-amplitude	K_1	31.18	0.12	km s^{-1}	
Velocity offset	$\gamma(SOPHIE)$	4.34	0.09	km s^{-1}	
Velocity offset	$\gamma(APO)$	-32.2	2.8	km s^{-1}	
Argument of Periapsis	ω	215.4	3.7	°	
Eccentricity	e	0.0244	0.001		

Table 3: Best-fit Parameters for Three Dynamical Models.

Binary Stars	Model 1	Model 2	Model 3	Uncertainty
Mass of Primary Star [$M_\odot$]	1.0	1.02	1.03	0.1
Mass of Secondary Star [$M_\odot$]	0.2614	0.2646	0.2662	0.03
Radius of Primary Star [$R_\odot$]	1.6	1.6	1.6	–
Radius of Secondary Star [$R_\odot$]	0.35	0.35	0.35	–
Semimajor Axis [AU]	0.1558	0.1567	0.1572	0.003
Circumbinary Planet				
Orbital Period [days]	137.82	138.2	137.89	0.05
Semimajor Axis [AU]	0.5644	0.5679	0.5695	0.005
Eccentricity	0.09	0.1	0.1	0.02
Argument of Periastron [degrees]	270	270	270	–
Orbital Inclination [degrees]	90	90	90	–

Table 4: Times, depths and durations of observed and predicted future planetary transits.

Event #	Center (BJD-2450000)	σ (Center)	Depth† [ppm]	σ (Depth)	Duration [days]	σ (Duration)	Center (Model1)	Duration (Model1)	Center (Model2)	Duration (Model2)	Center (Model3)	Duration (Model3)
Observed												
1	5070.8267	0.019	870	90	0.5485	0.0378	—	0.56	—	0.56	—	0.56
2	5207.4077	0.011	631	90	0.5125	0.021	5207.43	0.51	5207.42	0.50	5207.42	0.50
3	5344.1308	0.012	914	83	0.6184	0.023	5344.10	0.55	5344.12	0.55	5344.11	0.55
4	5480.004	0.015	1042	78	0.7513	0.029	5480.01	0.76	5480.04	0.74	5480.02	0.74
5	5613.2329	0.013	1043	67	0.891	0.032	5613.24	0.84	5613.21	0.82	5613.19	0.82
Predicted												
6	—	—	—	—	—	—	5749.08	0.51	5748.98	0.5	5748.97	0.5
7	—	—	—	—	—	—	5885.71	0.51	5885.57	0.5	5885.55	0.5
8	—	—	—	—	—	—	6022.20	0.6	6022.05	0.6	6022.02	0.6
9	—	—	—	—	—	—	6157.40	1.0	6157.24	1.0	6157.19	1.0

†: in terms of $(\frac{r_p}{r_A})^2$